



## The history of ground ice formation and intra-permafrost fluid flow as documented by Ra and Th isotopes

Dotan Rotem<sup>1,2</sup>, Yishai Weinstein<sup>1</sup>, Yehudit Harlavan<sup>3</sup>, Adi Torfstein<sup>4,5</sup>, Hanne H. Christiansen<sup>2</sup>

5 <sup>1</sup>Department of Environment, Planning and Sustainability, Bar-Ilan University, Ramat-Gan, 529002, Israel.

<sup>2</sup>Arctic Geophysics Department, the University Centre in Svalbard, UNIS, Longyearbyen 9170, Norway.

<sup>3</sup>Geological Survey of Israel, 32 Yesha'yahu Leibowitz, Jerusalem 9692100, Israel.

<sup>4</sup>Institute of Earth Sciences, Hebrew University of Jerusalem, Jerusalem, Israel.

<sup>5</sup>The Interuniversity Institute for Marine Sciences, Eilat, Israel.

10 *Corresponding to:* Dotan Rotem [dotanrotem1969@gmail.com](mailto:dotanrotem1969@gmail.com)

### Abstract

While permafrost is considered a permanently frozen soil, it often demonstrates evidence for internal processes, including fluid migration. Here, we present data of the chemical composition, Ra, Th and Ac isotopes of saline permafrost from three closely-retrieved cores drilled at Adventdalen, a fjord Valley in central Svalbard, which provides evidence for a fingering style intra-permafrost fluid flow. Ground ice of the different cores differs markedly in their salinity and composition. In one core, which has a composition similar to seawater, the long to short-lived isotope ratios, ( $^{226}\text{Ra}/^{223}\text{Ra}$ )<sub>AR</sub> and ( $^{226}\text{Ra}/^{224}\text{Ra}$ )<sub>AR</sub>, are relatively low, being similar to parent isotope activity ratios ( $^{230}\text{Th}/^{227}\text{Ac}$  and  $^{230}\text{Th}/^{228}\text{Th}$ , respectively) on grain surfaces (CEC fraction). Ground ice of the two other cores, which are less saline and have Na/Cl and SO<sub>4</sub>/Cl ratios higher than seawater, demonstrates much higher Ra isotope ratios, closer to parent ratios in the bulk sediment. It is suggested that the different isotope ratios are due to different residence times, and that the parameter controlling the isotope ratios is radium diffusion from inside the grains. While ground ice in the less saline cores was formed during permafrost formation (10-9 ka), ground ice average residence time in the more saline core is shorter, <<2,000 years, which did not allow a significant diffusion of the long-lived  $^{226}\text{Ra}$  from inside the grains. The latter is probably the result of a Late Holocene intrusion of saline fluids, arriving from a low-Th or high water:rock ratio basement rock. This highlights the internal dynamics of saline permafrost, which may affect its resilience to the ongoing global warming.

### 1. Introduction

30 Permafrost is a soil or rock that has remained at or below 0 °C for at least two consecutive years. While permafrost covers more than 20% of the northern hemisphere land area, it is evident that its distribution has dramatically declined during the last several decades, due to the ongoing global warming (Brown et al., 2002; Obu et al., 2019; Li et al., 2022), with continuous permafrost areas changing into discontinuous and sporadic permafrost zones (Kwong and Gan, 1994; Anisimov and Nelson, 1997; Osterkamp and Romanovsky, 1998; James et al., 2013).  
35 While some of the permafrost is very old and thick, in particular in inland settings, such as Siberia, Canada, Alaska, and Antarctica (Gilichinsky and Wagener, 1995; Dobinski, 2011; Abramov et al., 2021), other areas are dominated by young permafrost (Late Pleistocene to Holocene), related to the last deglaciation, which exposed vast areas to the atmosphere and opened the way for cooling and permafrost formation (e.g., Jin et al., 2007; French, 2007). Following exposure, permafrost aggradation may go two ways. The first, applied to the already deposited



40 sediments and bedrock, is the top-down, epigenetic permafrost formation, while the other is the bottom-up, syngenetic cooling and freezing of the newly deposited sediments.

Whereas most permafrost is significantly colder than 0°C, it is not necessarily strictly frozen (French, 2007; Dobinski, 2011; Keating et al., 2018), which is due to both the lowering of the freezing point in saline permafrost (Ahonen, 2001), as well as due to capillary or surface adsorption effects in the sediment pore space (e.g., Sheshukov and Nieber, 2011; Wang et al., 2020), which in turn could be related to water content and grain size (e.g., Zhang et al., 2018; Wang et al., 2021). The presence of fluids may boost intra-permafrost processes, allowing the re-distribution and migration of fluids in the cryotic pore space (Fisher et al., 2019; Lacelle et al., 2022).

Intra-permafrost processes are often associated with supra-permafrost processes, such as infiltration from the active layer (Mackay, 1983; Marsh and Woo, 1993; Boike et al., 1998), runoff on slopes to form foothill mounds (Åkerman and Malmström, 1986), intrusion from rivers (Alekseyev, 2015) and thaw-freeze crack-filling, which produce the commonly-observed ice wedges and polygon structures (e.g., Harry and Gozdzik, 1988; Mackay, 1989; Christiansen et al., 2005; Opel et al., 2018). On the other hand, intra-permafrost ice segregation is also common (Mackay, 1983; Mackay and Dallimore, 1992; Solomatin and Xu, 1994; Fu et al., 2022). While this is more difficult to trace, Weinstein et al., (2019) showed by Ra and Th isotopes, combined with <sup>3</sup>H, that a segregated ice layer at Adventdalen, central Svalbard (Fig. 1), had been formed very recently (less than one year).

Naturally, due to its lower freezing temperature, saline permafrost (i.e., soils with significant content of soluble salts, such that results in a freezing point depression, e.g., Banin and Anderson, 1974; Marion, 1995) is more prone to fluid migration and intra-permafrost processes. Near-surface saline permafrost is widely distributed in the northern circumpolar region, especially in the continuous permafrost zone, covering up to 35% of that area (Brouchkov, 2002). The salinity source is commonly related to seawater (Hivon and Segó, 1993; Brigham-Grette and Hopkins, 1995; Forman et al., 2004; Lønne and Nemeč, 2004; Jones et al., 2023), although it can also be strictly terrestrial, related to evaporation processes in inland basins and to water-rock interaction (e.g., Dickinson and Rosen, 2003; Henkemans, 2016; Gao et al., 2017). Salinity and cryotic state (i.e., freezing degree of the pore fluid) are highly heterogeneous in the saline permafrost environment (e.g., Brouchkov, 2002; Ahonen, 2001; Dafflon et al., 2016). This heterogeneity is sometimes manifested by the presence of lenses of unfrozen ground or overcooled brines ('cryopegs'), which usually form due to freezing and salt expulsion processes (e.g., Yerшов, 1998; Iwahana et al., 2021).

In Svalbard, near-surface saline permafrost is commonly observed in fjord valleys, where seawater ingression occurred during the early Holocene, following glacial retreat and sea level rise (e.g., Cable et al., 2018; Gilbert et al., 2019; Rotem et al., 2023). Permafrost formation has been inhibited until after seawater regression and the exposure of the recently deposited sediments to the atmosphere (Gilbert et al., 2018). The actual formation of the permafrost depends on the combination of climatic and soil physical attributes. Accordingly, while Hornum et al., (2020) argued that freezing at Adventdalen (Fig. 1) did not occur until 4500 years BP due to the relatively warm mid-Holocene, Rotem et al., (2023) suggested that permafrost started forming immediately after exposure (ca. 9 ka), which was assisted by the thermal conductivity difference between solid ice and liquid water. In this paper, we show by chemical composition and radioisotopes that the permafrost in eastern Adventdalen demonstrates a complex and multi-stage history of ground ice formation.

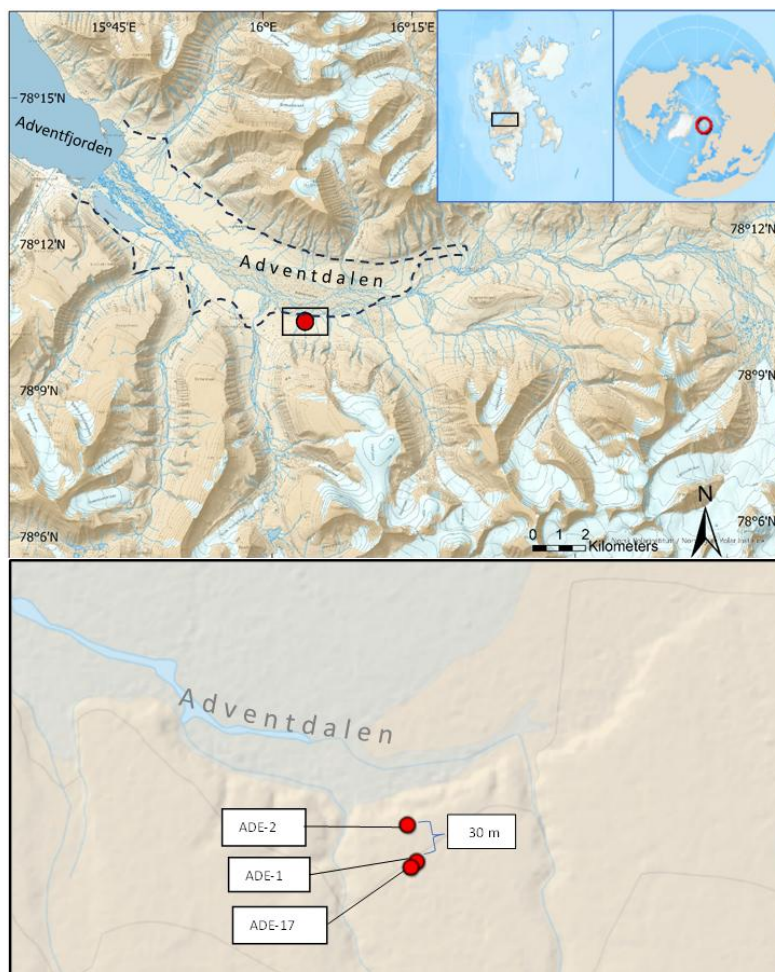


**Figure 1:** Location and detailed map of the ADE study site. The dashed line represents sea ingression limit at the early Holocene (Lønne and Nemeč, 2004, drawn after Hodson et al., 2020). The map is provided with courtesy of the Norwegian Polar Institute.

80

### 1.1 Radium isotopes

In this work, we report the activities (i.e., concentrations) of radium isotopes in ground ice, as well as their radioactive parents (thorium and actinium) in the permafrost sediments. Radium has four naturally occurring isotopes:  $^{223}\text{Ra}$ ,  $^{224}\text{Ra}$ ,  $^{226}\text{Ra}$ , and  $^{228}\text{Ra}$ . All isotopes are produced by decay chains, stemming from  $^{238}\text{U}$ ,  $^{235}\text{U}$ , and  $^{232}\text{Th}$  (Fig. 2). Specifically, all Ra isotopes are produced by the  $\alpha$  decay of different Th (thorium) isotopes ( $^{227}\text{Th}$ ,  $^{228}\text{Th}$ ,  $^{230}\text{Th}$  and  $^{227}\text{Th}$ , respectively), although in the case of  $^{223}\text{Ra}$ , we mainly relate to its ‘grandparent’  $^{227}\text{Ac}$ , due to the short life of its direct parent  $^{227}\text{Th}$  (half-life: 18.7 days). An important aspect is that while thorium (parent isotopes) is a particle-reactive element (i.e. in the presence of water, it will always be on the solids), radium is much more mobile in water. The  $^{226}\text{Ra}$  is the longest-lived radium isotope, with a half-life of 1601 years,  $^{228}\text{Ra}$  has

90



5.8 years, while  $^{224}\text{Ra}$  and  $^{223}\text{Ra}$  are short-lived, with half-lives of 3.66 and 11.4 days, respectively (Bourdon et al., 2003). The wide range of half-lives of the radium isotopes allows their application to various processes with very different time scales. For example, for short-term groundwater processes,  $^{228}\text{Ra}$ ,  $^{223}\text{Ra}$ , or  $^{224}\text{Ra}$ , and their activity ratios are good tracers (e.g., Moore, 2003; Hsieh et al., 2013). However, for a distinction between thawed ground ice and active layer water or between young and old sub-permafrost groundwater,  $^{226}\text{Ra}$  would be a better tracer, since its growth toward equilibrium with its parent nuclide,  $^{230}\text{Th}$ , takes 5-6 half-lives (8-10,000 years; e.g., Weinstein et al. 2019; Rotem et al., 2024).

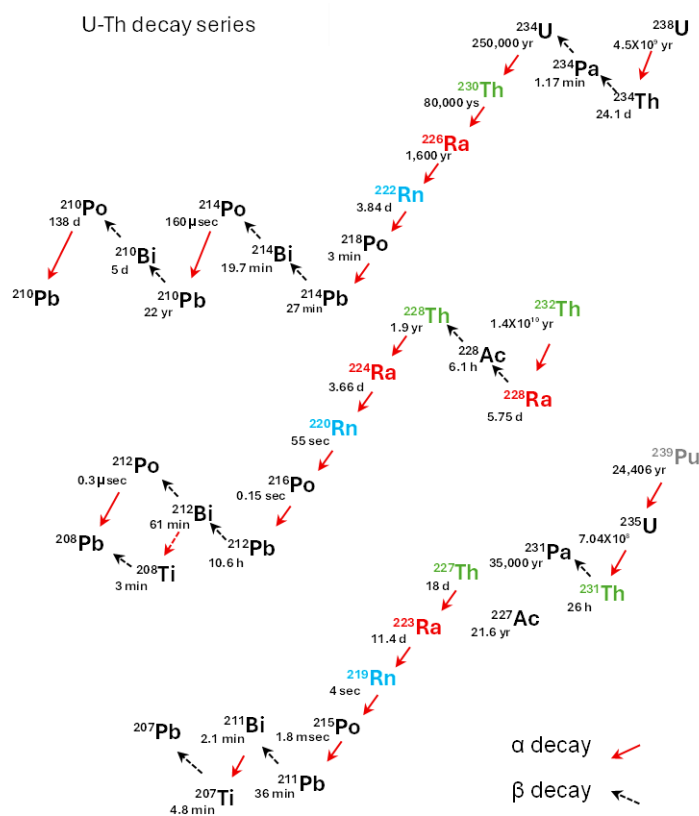


Figure 2: The three U-Th decay series. Radium isotopes are designated red and Thorium is labelled green. Note that all Ra isotopes are produced by a decay of Th isotopes, and that two of the four Ra isotopes are along the  $^{232}\text{Th}$  decay chain.

## 100 2. Study site

The data presented in this study are from cores drilled into the permafrost in the Adventdalen Valley (hereafter Adventdalen), Svalbard (Fig. 1), during March 2017 and March 2022. The Adventdalen is a U-shaped fjord valley, carved by advancing and retreating glaciers. During the last glacial cycle, it was eroded to its basement (Elverhøi et al., 1994), which was followed by Early Holocene glacier retreat and seawater ingress up valley (Lønne and



105 Nemeč 2004), resulting in the deposition of deltaic sediments (Gilbert et al., 2018). A relatively fast elastic rebound  
(Forman et al., 2004) resulted in the exposure of the sediments to the atmosphere, starting at the eastern part of the  
valley ca. 9.5 ka and arriving at the current coastline location no later than 4 ka (Gilbert et al., 2018). The exposed  
sediments froze epigenetically within a short time after exposure to the atmosphere (100s years; Rotem et al.,  
2023). The marine sediments were then covered by several meters of mid to Late Holocene fluvial sediments,  
110 which were overlain by 2-3 m of aeolian deposits, and both went through syngenetic freezing (Gilbert et al., 2018).  
At present, the thickness of the permafrost in the valley is estimated at less than 100 m next to the coast (Humlum  
et al., 2003) and up to 250 m up-valley (Isaksen et al., 2001), most of it being epigenetic and the shallow 4-5 m  
syngenetic, while active layer depth ranges between 0.5-1 m (Christiansen et al., 2005; Weinstein et al., 2019).  
Permafrost in Svalbard is considered continuous (Obu et al., 2019), although non-frozen and partially frozen  
115 permafrost were also reported (Keating et al., 2018; Weinstein et al., 2019), and recent works about sub-permafrost  
hydrology also question the continuity of the permafrost in this area (e.g., Rotem et al., 2024).

Four boreholes were drilled at the ADE site, a river terrace, 23 m a.s.l., 9.8 km up-valley from the Adventfjorden  
(Fig. 1). Two closely spaced (0.5 m apart) boreholes, centered at 78.17220N 16.06130E, were drilled during spring  
2017, and they are treated here as one core, ADE-17. The other two cores, ADE-1 and ADE-2 were drilled in  
120 spring 2022. ADE-1 is located within a few meters from ADE-17 (78.17216N 16.0610E) and ADE-2 was drilled  
ca. 30 m away (78.17243170N 16.06114840E). The valley-fill section at the site (14-20 m, Gilbert et al., 2018 and  
this study) consists of 1.5 m of fine-grained aeolian deposits underlain by fluvial gravel down to 5.5 m, which  
in turn is underlain by deltaic sediments (ca. 12 m). The Holocene section covers glacial sand deposits, 2.5 m thick  
(Gilbert et al., 2018), which are underlain by basement rocks (Lower Cretaceous, shales) (Grundvåg et al., 2019).

125

### 3. Methods

The drilling campaigns were executed using the University Center in Svalbard (UNIS) permafrost drill rig (Gilbert  
et al., 2018), using core barrels of 43 mm diameter (ID) in 2017 and 58 mm in 2022. The two boreholes drilled in  
2017 reached depths of 13 and 9 m, while the 2022 ones (ADE-1 and -2) reached a depth of 16 m. In the latter, the  
130 bottom 1-2 m was composed of bedrock, which was excluded from sample processing. The upper 5 m (syngenetic  
part) of ADE-2 was drilled with a jackhammer. While the extracted cuttings have been analyzed, the results are  
not presented in this study due to possible downhole contamination. Core length, borehole depth, core freezing  
status, and gravel content were recorded in the field. Retrieved core sections were sealed in plastic bags and stored  
frozen at  $-18\text{ }^{\circ}\text{C}$  at UNIS. The cores were subsequently sectioned in a cold room ( $-5\text{ }^{\circ}\text{C}$ ) into 0.5–1 m depth  
135 intervals. Subsamples were scraped and crushed into small fragments, which were transferred to 250 ml centrifuge  
tubes. For samples with low water (ice) content, up to 40 ml of Ra-free water was added to facilitate porewater  
extraction. The samples were then thawed in a microwave oven at 600 W for 2 min and centrifuged for 8 min at  
11,000 rpm (high g) to separate the meltwater from the soil matrix. The extracted water was sequentially filtered  
through 3  $\mu\text{m}$  and 0.45  $\mu\text{m}$ . Net water volumes extracted varied strongly (in accordance with the high variability  
140 of ice content) and summed to 42-1391 ml per sample. It is important to note that in this paper, we consider all  
extracted water as thawed ground ice, although some of the core segments were not fully frozen, thus liquid water  
could also be present to a certain amount, especially in the more saline samples (see Keating et al., 2018; Weinstein  
et al., 2019). We also note that the mentioned addition of Ra-free water to samples with low ice content could  
result in some desorption from grain surfaces, as well as in salt dissolution when exists. Yet, both salts and



145 adsorbed ions are assumed part of the pore space chemical composition (see a similar conception by Ewing et al., 2015, regarding U isotopes in ground ice).

Most of the extracted water was used for Ra isotope analysis, while 30-60 ml was used for elemental chemistry analyses. For Ra isotopes, The solution was run 3-5 times through manganese-coated fibers in order to adsorb the radium. Samples with pH lower than 6 were pre-treated by adding a low concentration NaOH solution (Ra-free).  
150 Sample water was also run through a secondary Mn-coated fiber as to account for Ra adsorption efficiency on the fibers. In six samples (DR-AD-121-126), the adsorption efficiency was determined by measuring and comparing  $^{226}\text{Ra}$  on both fibers and water samples. Efficiencies were very variable, from 90% down to <50%, with the lower end being probably due to relatively low pH and/or reducing conditions, and in certain samples due to high salinity, all tend to reduce Ra adsorption (e.g. Gonneea et al. 2008; Kiro et al. 2012). Measured activities of all isotopes  
155 were corrected accordingly, assuming no mass-dependent fractionation. Nevertheless, due to the uncertainties about both extraction protocol and adsorption efficiency on the fibers, in this paper, we mainly focus on isotope ratios as all isotopes are affected the same by adsorption efficiency.

The radium adsorbed on the fibers was then measured for the short-lived  $^{224}\text{Ra}$  by the RaDeCC system (Moore and Arnold, 1996) within 2-3 days after water-soil separation, while  $^{223}\text{Ra}$  was measured after ca. 10 days, as to minimize the cross-talk between  $^{224}\text{Ra}$  and  $^{223}\text{Ra}$ .  $^{224}\text{Ra}$  was re-measured after 3-4 weeks after reaching equilibrium with its radioactive parent  $^{228}\text{Th}$ . Fibers were measured for  $^{226}\text{Ra}$  by an emanation system and Lucas Cells (Mathieu et al., 1988) after a 3-week incubation, to allow for  $^{222}\text{Rn}$  equilibration with  $^{226}\text{Ra}$ .  $^{228}\text{Ra}$  was measured by a low background well-type HPGe gamma spectrometer (Canberra), using the 911 KeV peak of  $^{228}\text{Ac}$ . All results are presented as dpm (disintegrations per minute) per liter of thawed ground ice, which can change strongly due to the  
160 ice content of the permafrost. Analytical errors on  $^{226}\text{Ra}$ ,  $^{228}\text{Ra}$ , and  $^{224}\text{Ra}$  were commonly  $\leq 10\%$ , while those of the low activity  $^{223}\text{Ra}$  were in certain cases up to  $>30\%$  (Weinstein et al., 2019).

The Radium isotopes accumulate in the frozen pore space following recoil from their parent nuclides Th and Ac, which are located either on or within the sediment grains. Accordingly, thorium isotopes and  $^{227}\text{Ac}$  were measured both in the bulk grains and in the adsorbed fraction of the permafrost sediment, after thawing and completing the  
170 ground ice-soil separation. Several grams of soil samples were disaggregated and homogenized in an agate mortar for the bulk sediment analysis. For the bulk sediment measurements, 0.3 g of each sample was placed in a Teflon beaker and was treated with 1 ml HF and 5 ml  $\text{HNO}_3$  (both concentrated, ultrapure grade). A droplet (ca. 0.035 ml) of a  $^{229}\text{Th}$  spike (86 ppt) was added to the solution and the beakers were placed on a hot plate (200 °C) to let evaporate. The residue was then treated with 5 ml HCl. A few drops of  $\text{H}_2\text{O}_2$  were added to remove the organic matter content. The adsorbed fraction was determined by the CEC (Cation Exchange Capacity) measurement. A sediment sample of five grams was shaken with 25 ml of ammonium acetate for 16 hours. Sample was then centrifuged, and the liquid phase was evaporated. The final products of both protocols (bulk and CEC) were dissolved in 7 N  $\text{HNO}_3$  (6 ml, and 2 ml, respectively). Solutions (2 ml) were run via Bio-Rad AG 1X8 200-400 mesh resin, following the protocol for Thorium ion chromatography separation (Grant et al., 2012).  $^{230}\text{Th}$  and  
175  $^{232}\text{Th}$  (radioactive parents of  $^{226}\text{Ra}$  and  $^{228}\text{Ra}$ , respectively) were determined by a Neptune Plus Multicollector ICPMS at the Institute of Earth Science, The Hebrew University of Jerusalem.  $^{228}\text{Th}$  and  $^{227}\text{Ac}$  (parents of  $^{224}\text{Ra}$  and  $^{223}\text{Ra}$ , respectively) were studied separately by the RaDeCC system (Moore and Arnold, 1996), assuming equilibrium has been achieved with their short-lived radium isotope. Results are presented as dpm  $\text{g}^{-1}$  sediment.  
180



185 Analytical errors for the MC-ICPMS thorium measurements were up to 2% for the bulk sediment and 0.5% for  
the CEC, while RaDeCC errors for  $^{228}\text{Th}$  and  $^{227}\text{Ac}$  were up to 17% and 30%, respectively, due to the low counts.  
Major elements were analyzed at the Geological Survey of Israel (GSI). Cations and  $\text{SO}_4^{2-}$  were measured by  
inductively coupled plasma atomic emission spectroscopy (ICP-OES; Optima 5300). The  $\text{Cl}^-$  concentrations were  
determined according to their concentration in the solutions; above 50 ppm via potentiometer titration (Metrohm  
702 SM Titrino titrator connected to a chlorine electrode) or below 50 ppm by Ion Chromatograph, which was  
190 also used for  $\text{Br}^-$  concentrations. Bicarbonate was analyzed as alkalinity via titration. The analytical error for all  
majors is less than 5%. We note that the chemical composition of ground ice in ADE-17 was already presented in  
Rotem et al., (2023). Ice content, defined as gravimetric moisture content  $(W-D)/D \times 100$ , where W and D refer  
to the wet and dry sample mas (Gilbert et al., 2018).

## 195 4. Results

### 4.1. Ground-ice chemical composition

Ice content (frozen water mass divided by dry mass) of the samples varied strongly, from 2% to >180% (180% ice  
content translates into 64% water content), and was, in general, higher in the shallow, syngenetic part (Table C1,  
Appendix A). Ground-ice (i.e., water extracted from thawed permafrost) chemical composition of the syngenetic  
200 section (ADE-17 and ADE-1) is basically that of fresh water with typical TDS concentrations of 100-200  $\text{mg l}^{-1}$   
(Table C1), while ionic ratios of major elements to  $\text{Cl}^-$  are higher than that of seawater (e.g.,  $\text{Na}/\text{Cl}$  of 1.01-3.58,  
Figs. 3 and 4). On the other hand, ground ice in the epigenetic section, deeper than 5-5.5m, is mostly brackish to  
saline, which varies between the cores. While in ADE-1 and ADE-17,  $\text{Cl}^-$  concentration is <2,400 and <3,700  $\text{mg l}^{-1}$ ,  
respectively, in ADE-2 it is significantly higher (up to 7,900  $\text{mg l}^{-1}$ ), with one outlier (DR-AD-125 from ADE-  
205 2) as high as 22,732  $\text{mgCl}^- \text{l}^{-1}$  and 14,333  $\text{mgNa}^+ \text{l}^{-1}$  (Table C1). In ADE-17,  $\text{Cl}^-$  and other major elements show a  
mixing pattern with depth, with concentrations increasing from 438  $\text{mgCl}^- \text{l}^{-1}$  at 5.5 m to 2,150-3,680  $\text{mgCl}^- \text{l}^{-1}$  at  
9-12 m (Figs. 3a-e). This is not observed in ADE-2, where high salinities are observed up to the top of the  
epigenetic section. Unlike  $\text{Cl}^-$ , the  $\text{Ca}^{+2}$  does not show any pattern with depth in ADE-17, and concentrations in  
the epigenetic section are similar to those in the syngenetic one (Fig. 3f).

210 Ion ratios vary along the profile. While in the syngenetic part,  $\text{Na}/\text{Cl}$  and  $\text{SO}_4/\text{Cl}$  are mostly much higher than in  
seawater (equivalent ratios up to 3.60 and 1.77, respectively, Figs. 4 and 5a-b, no data for ADE-2), in the epigenetic  
part, ratios are  $\leq 2$  and  $\leq 0.45$ , respectively (Figs. 5a-b). Nevertheless, in ADE-17 and ADE-1, ratios at the shallow  
part of the epigenetic section (6-10 m) are also relatively high (up to 1.92 and 0.45, respectively), showing a rough  
continuum with the deep part of the syngenetic section (Figs. 5a-b). On the other hand, in ADE-2 (epigenetic  
215 section) ratios are more uniform, with  $\text{Na}/\text{Cl}$  equivalent ratios similar to that of seawater (0.84-1.02) and  $\text{SO}_4/\text{Cl}$   
mostly lower than that of seawater ( $\leq 0.1$ , Figs. 4 and 5a-b).  $\text{Ca}/\text{Cl}$ ,  $\text{Mg}/\text{Cl}$ , and  $\text{K}/\text{Cl}$  generally show similar  
patterns, with very high  $\text{K}/\text{Cl}$  and, to a lesser extent  $\text{Ca}/\text{Cl}$  in the syngenetic part, while close to seawater ratios in  
the epigenetic part of the profile, this time in all cores (except for the highly saline DR-AD-125, Figs. 5c-d).

220



225

230

235

240

245

250

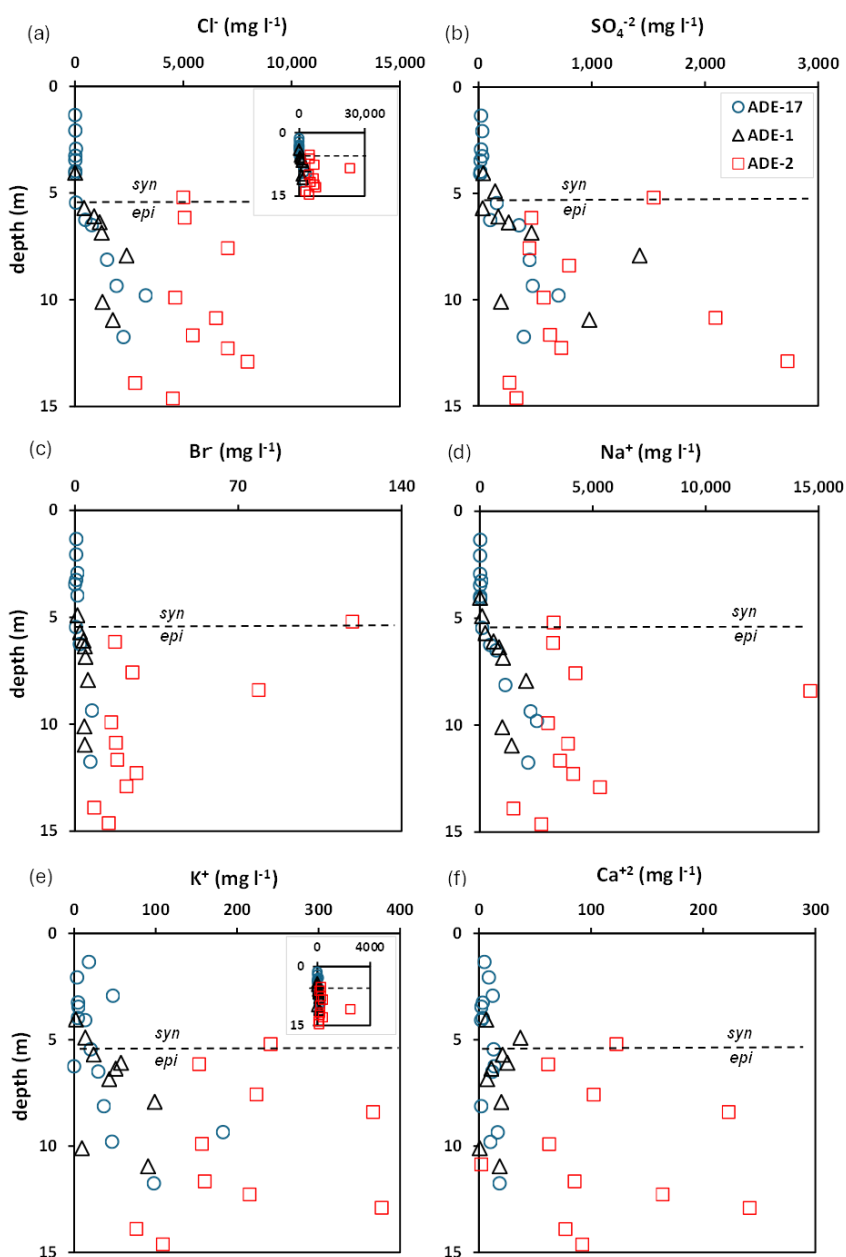


Figure 3: Concentration of selected major elements along the profile of the three ADE cores (ADE-17, ADE-1, and ADE-2). The dashed line shows the boundary between syngenetic (*syn*) and epigenetic (*epi*) permafrost at the site (Gilbert et al., 2018). The insets in the Cl<sup>-</sup> and K<sup>+</sup> diagrams are for sample DR-AD-125 and DR-AD-150, respectively.



255

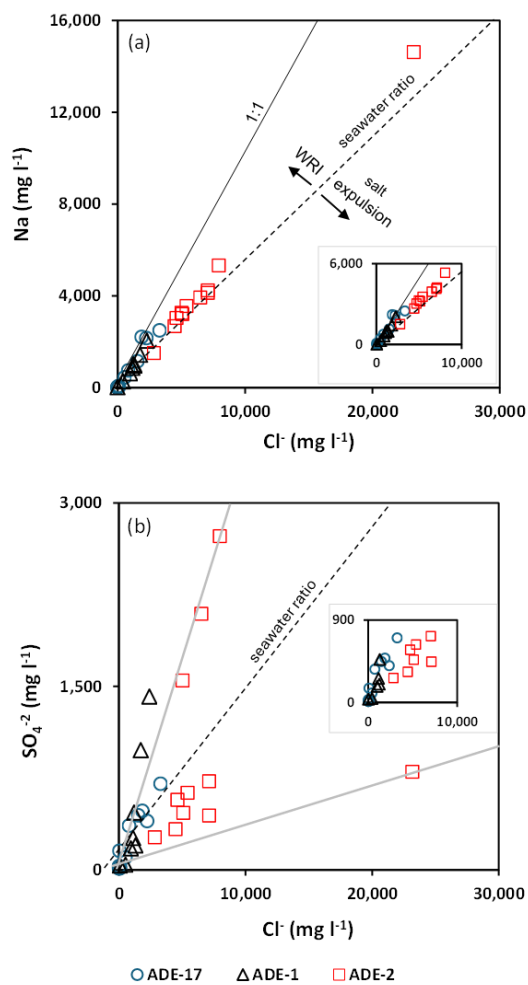


Figure 4: (a) Sodium and (b) sulphate against chloride in the ground ice of the ADE cores. WRI refers to Water-Rock Interaction.

260

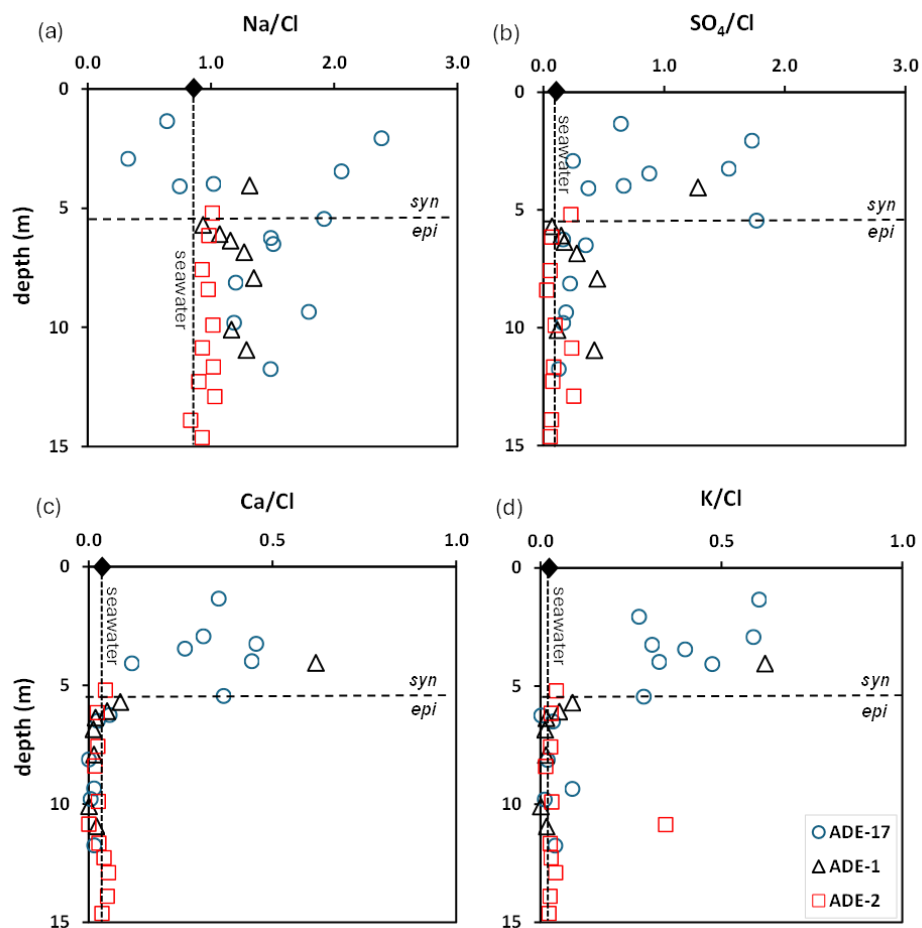


Figure 5: Ground ice equivalent ratios in the ADE cores. The black full diamond and vertical dashed line is for seawater composition (de Baar et al., 2017, Salinity of 35 ppt). The horizontal dashed line as in Figure 3.

265

270



275 4.2. Radium isotopes in ground ice

Radium isotope activities are presented in Table C2. Activities of  $^{226}\text{Ra}$ ,  $^{228}\text{Ra}$ , and  $^{224}\text{Ra}$  in ground ice are quite similar, varying between  $<1$  to  $60 \text{ dpm l}^{-1}$  (averages of  $10\text{-}13 \text{ dpm l}^{-1}$ ), while  $^{223}\text{Ra}$  is an order of magnitude lower, with an average of  $0.7 \text{ dpm l}^{-1}$  (Fig. 6a-d). Activities of  $^{224}\text{Ra}$  and  $^{223}\text{Ra}$  are fairly uniform with depth in ADE-17 and ADE-1 (although  $^{224}\text{Ra}$  is slightly higher in the epigenetic section), while activities in the more saline ADE-2 samples (epigenetic) are significantly higher (Figs. 6a- b and 7). On the other hand,  $^{226}\text{Ra}$  is similar in all three cores, showing no trend with depth, although the highest activities in ADE-17 were observed at the top of the epigenetic section (Fig. 6c).  $^{228}\text{Ra}$  activities are higher in the epigenetic section (Fig. 6d).

280

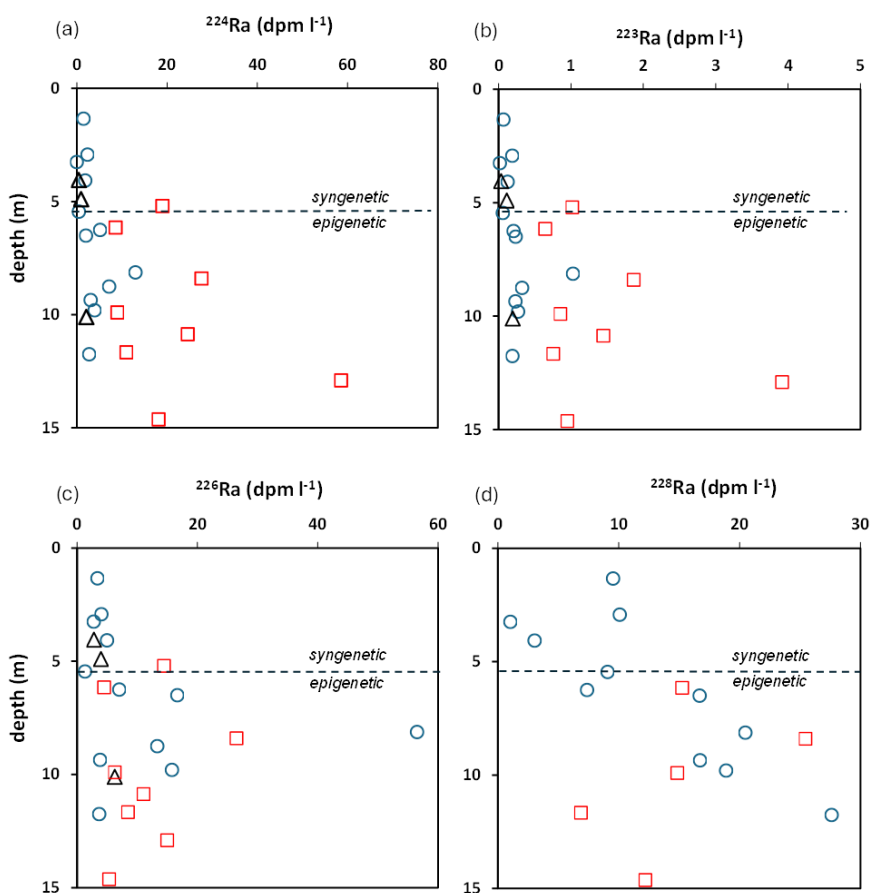


Figure 6: Radium isotope activities in ground ice of the three ADE cores. The dashed line as in Figure 3

Ratios of the long to short-lived radium isotopes,  $(^{226}\text{Ra}/^{223}\text{Ra})_{\text{AR}}$ , demonstrate a large range (4 to 72; Fig. 8a, with three outliers  $>100$ ). Nevertheless, there are marked differences between the cores. While in ADE-17 and ADE-1,  $(^{226}\text{Ra}/^{223}\text{Ra})_{\text{AR}}$  ratios both in syngenetic and the epigenetic section are close or higher than the secular equilibrium activity ratio (21.7, which is the natural ratio of parent nuclides  $^{238}\text{U}/^{235}\text{U}$ , e.g., Kiro et al., 2015; Weinstein et al., 2021), ratios in ADE-2 (epigenetic section) are relatively low, ranging between 4-14 (Figs. 7c and 8a).

285

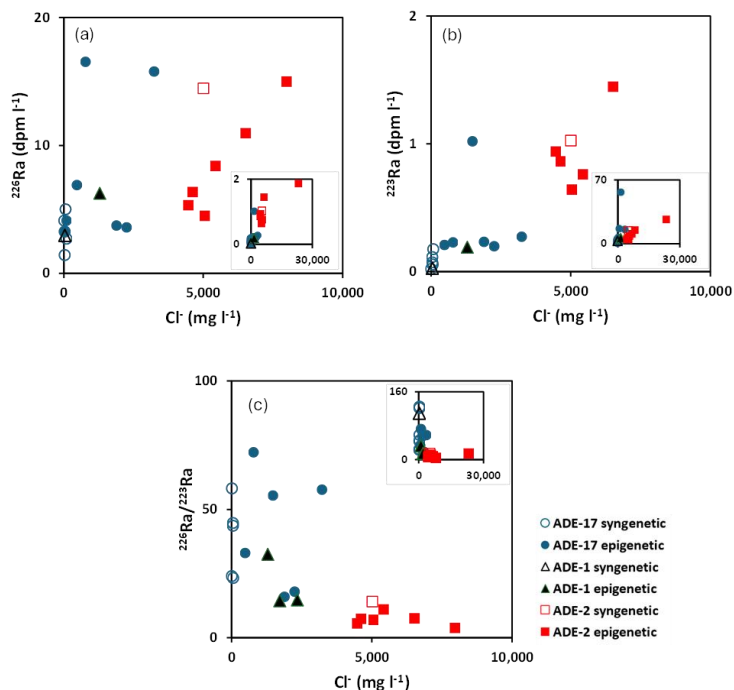


Figure 7: Radium isotope activities and ratios against chloride. (a) <sup>223</sup>Ra, (b) <sup>226</sup>Ra, (c) <sup>226</sup>Ra/<sup>223</sup>Ra.

290

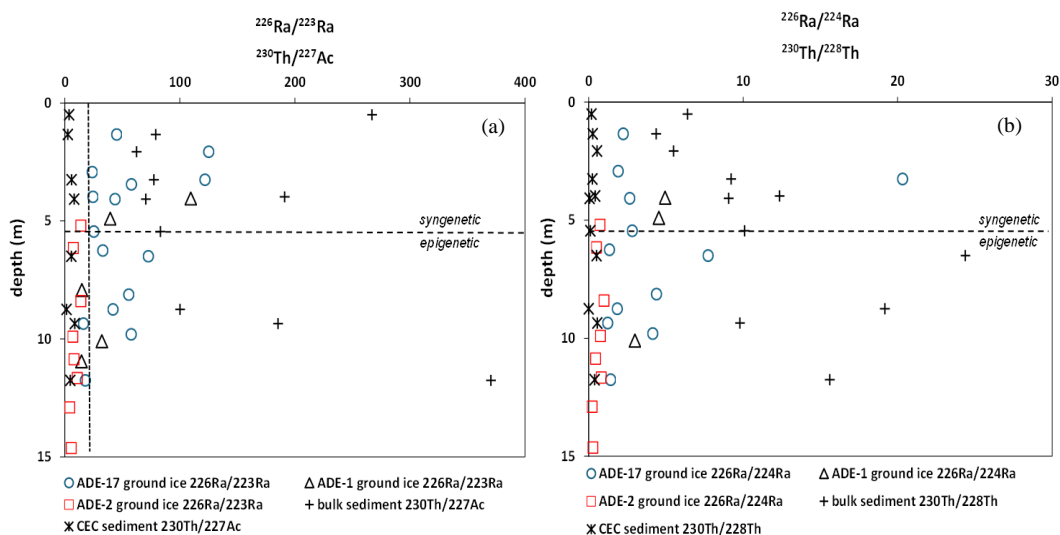


Figure 8: Radium isotope activities in ground ice and their parent ratios in bulk soil grains and on grain surfaces (CEC, for Cation Exchange Capacity). (a) (<sup>226</sup>Ra/<sup>223</sup>Ra)<sub>AR</sub> and (<sup>230</sup>Th/<sup>227</sup>Ac)<sub>AR</sub>; (b) (<sup>226</sup>Ra/<sup>224</sup>Ra)<sub>AR</sub> and (<sup>230</sup>Th/<sup>228</sup>Th)<sub>AR</sub>. The vertical dotted line in (a) indicates the secular equilibrium ratios of (<sup>235</sup>U/<sup>238</sup>U), parents of <sup>226</sup>Ra and <sup>223</sup>Ra, respectively. The dashed line as in Figure 3.



295  $(^{226}\text{Ra}/^{224}\text{Ra})_{\text{AR}}$  shows a similar pattern, where ratios in ground ice from cores ADE-17 and ADE-1 are higher than those in ADE-2 samples ( $>1$  and  $0.3-1$ , respectively, Fig. 8b). The ratio of  $^{226}\text{Ra}$  to the medium-lived (half-life of 5.75 years)  $^{228}\text{Ra}$  is mostly  $\leq 1$ , with no difference between the cores (Table C3), although some of the ADE-17 samples show ratios  $\gg 1$ . The daughter-parent ratio  $(^{224}\text{Ra}/^{228}\text{Ra})_{\text{AR}}$  in ADE-17 ranges between 0.13-0.68 (outlier of 1.0), while in ADE-2 ratios in the epigenetic part are mostly higher (0.55-1.58, Fig. 9).

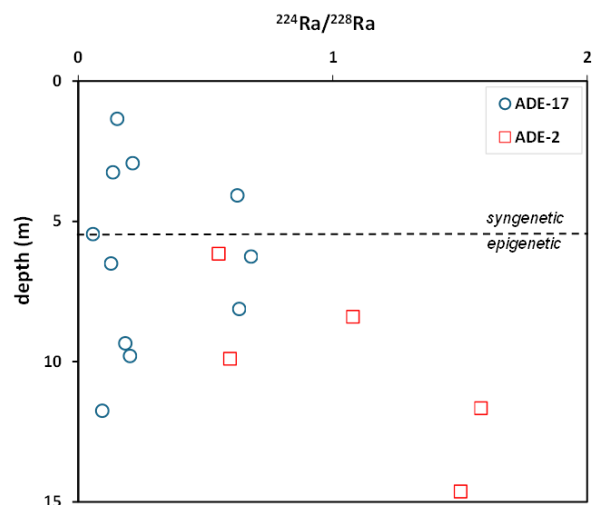


Figure 9:  $(^{224}\text{Ra}/^{228}\text{Ra})_{\text{AR}}$  in the ADE cores. The dashed line as in Figure 3.

#### 4.3. Thorium isotopes and $^{227}\text{Ac}$ in permafrost soil

300 Thorium isotope activities in soil samples (bulk and CEC) from core ADE-17 are presented in Table C3. While  $^{232}\text{Th}$  and  $^{230}\text{Th}$  activities in bulk samples are two to three orders of magnitude higher than in the CEC fraction (4.3-8.4 and 0.01-0.17 dpm  $\text{g}^{-1}$ , respectively),  $^{228}\text{Th}$  activities in the CEC are similar to those in the bulk (both are in the range of 0.1-1.2 dpm  $\text{g}^{-1}$ , Table C3 and Fig. 10), implying that most of the latter is adsorbed onto grain surfaces. This is also true for  $^{227}\text{Ac}$  (Table C3), where CEC activities are close (though lower) to bulk activities.

305 This is especially true for the epigenetic section, while in the syngenetic part, bulk sediment  $^{228}\text{Th}$  is up to 12 times that in the CEC (i.e., grain surface  $^{228}\text{Th}$  is not dominant, Fig. 10), although still lower from bulk/CEC ratios of  $^{232}\text{Th}$  and  $^{230}\text{Th}$  ( $10^2$ 's to  $100^2$ 's, Fig. 10).

$(^{230}\text{Th}/^{232}\text{Th})_{\text{AR}}$  in the bulk sediment is quite uniform along the whole permafrost section, ranging between 0.7-1.0 (Table C3). Ratios in the CEC fraction change from  $<1$  in the syngenetic permafrost to  $>1$  in the epigenetic section (5 – 12 m depth).  $(^{230}\text{Th}/^{227}\text{Ac})_{\text{AR}}$  in bulk sediment are significantly higher than the secular equilibrium activity ratio (21.7, Fig. 8a), while all CEC samples show lower than equilibrium ratios (2-12, Table C3, and Fig. 8a). This difference is apparently due to the high concentration of  $^{227}\text{Ac}$  on grain surfaces. Notably, daughter ratios,  $(^{226}\text{Ra}/^{223}\text{Ra})_{\text{AR}}$  in ground ice of ADE-2 is similar (slightly higher) to the  $(^{230}\text{Th}/^{227}\text{Ac})_{\text{AR}}$  in the CEC fraction, while in ADE-17  $(^{226}\text{Ra}/^{223}\text{Ra})_{\text{AR}}$  is much higher, 'mid-way', between CEC and bulk sediment ratios (Fig. 8a).

315  $(^{230}\text{Th}/^{228}\text{Th})_{\text{AR}}$  shows a similar pattern, with CEC ratios being much lower than the bulk sediment ratios, and with the daughter  $(^{226}\text{Ra}/^{224}\text{Ra})_{\text{AR}}$  in the ground ice of ADE-2 being similar to the CEC parent ratios and those of ADE-17 and ADE-1 positioned mostly between CEC and the bulk sediment ratios (Fig. 8b).

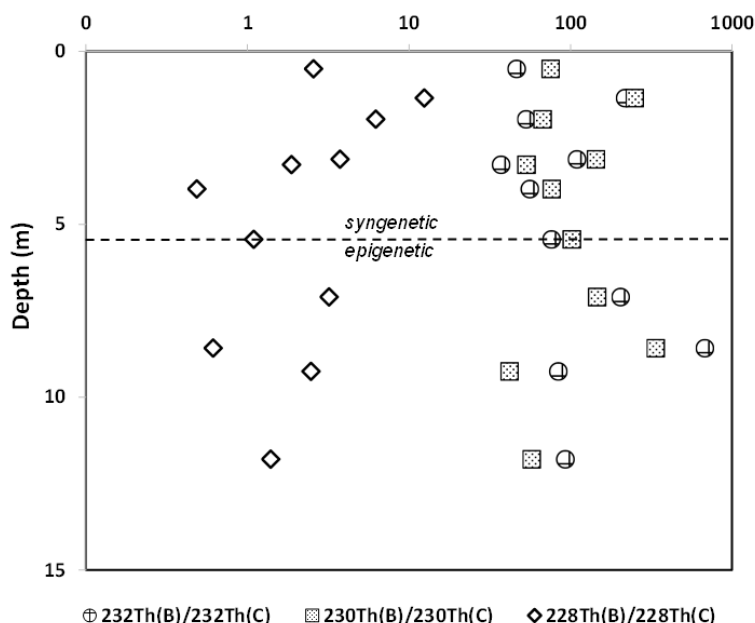


Figure 10: Bulk sediment/CEC (B/C) activity ratios of thorium isotopes in sediments from ADE-17. The dashed line as in Figure 3. Note the logarithmic scale.

320

## 5. Discussion

### 5.1. The heterogeneous nature of ground ice in Adventdalen

Our study site is located within the reach of the marine early Holocene transgression (Fig. 1, Gilbert et al., 2018), suggesting a-priori that the saline water observed in the permafrost epigenetic section is of an estuary-marine origin. Nevertheless, ground ice retrieved from the same depths in the three cores, located  $\leq 30$  m apart (Fig. 1), differ markedly in their salinity and composition, as well as in their radium isotope ratios (Figs. 3-8). The salinity of ground ice from borehole ADE-2 is relatively high, with up to seawater salinity and no distinct pattern with depth (Fig. 3). In ADE-17, salinity does not exceed 20% that of seawater, and it increases with depth in the epigenetic section. Finally, in ADE-1, salinity is less than 6-7% that of seawater, and no distinct pattern is observed. The difference between the cores is not just about the extent of dilution with fresh water/ground ice, but also about the contribution of water:rock interaction, as demonstrated by the ionic ratios. While in ADE-2, ionic ratios are relatively similar to seawater (Figs. 4 and 5; although Na/Cl of 1 could indicate halite dissolution in some of the samples and high  $\text{SO}_4/\text{Cl}$  in two of the samples could be due to sulfide oxidation, possibly related to the coal layers, common in the nearby slopes), ground ice from ADE-17 and ADE-1 shows Na/Cl and  $\text{SO}_4/\text{Cl}$  significantly higher than in seawater (although still lower than in the syngenetic part; Figs. 4 and 5a-b). The similar to seawater chemical composition in ADE-2 ground ice favors a marine source for its saline component. The  $>1$  Na/Cl in ADE-17 and ADE-1 (compared with 0.86 in seawater) suggests that, although probably also contains a seawater



component, porewater in these two cores went through significant water-rock interaction (WRI, e.g., dissolution  
340 or ion exchange). Accordingly, this water is the result of both mixing between fresh, meteoric water and Early  
Holocene seawater and of WRI. It should be noted that seawater freezing and saline fluid expulsion could not be  
a significant player here, since in this case fractionation would result in Na/Cl ratios lower than that of seawater  
(e.g., Herut et al., 1990), which is not the case in any of the samples (see fresh-seawater mixing line in Fig. 4a).  
The observation of a high salinity profile in ADE-2 all the way to the top of the epigenetic, marine section could  
345 be the result of an immediate freezing following exposure to the atmosphere (e.g., Rotem et al., 2023), which  
limited mixing with fresh water, as well as reduced the effect of WRI. However, the fact that this profile is very  
different from the nearby boreholes, including its salinity, chemical composition and pattern with depth, favors a  
later introduction of saline water into the permafrost pore space at this location, which could occur either via  
intrusion or by intra-permafrost segregation processes (e.g., Ahonen, 2001; French, 2007; Iwahana et al., 2021).  
350 Our radium results, support this post-permafrost formation scenario, as follows.

## 5.2. Radionuclides insights into ground ice timing

The differences in chemical composition between the cores are accompanied by differences in the Ra isotope  
ratios, where long to short-lived isotope activity ratios ( $^{226}\text{Ra}/^{224}\text{Ra}$  and  $^{226}\text{Ra}/^{223}\text{Ra}$ ) are significantly lower in the  
355 ground ice of ADE-2, compared with that in ADE-17 and ADE-1 (Figs. 8a-b). In particular, while  $(^{226}\text{Ra}/^{223}\text{Ra})_{\text{AR}}$   
in ADE-17 and ADE-1 are  $\geq 20$ , in ADE-2 these ratios are  $\leq 14$  (Fig. 8a). The low ratios in ADE-2 are apparently  
because activities of the short-lived isotopes are significantly higher than in the two other cores (Fig. 6b), while  
 $^{226}\text{Ra}$  activities are quite similar (Fig. 6a). However, the significantly higher salinity in ADE-2 should result in  
higher activities of all radium isotopes in this core due to the reduced adsorption (e.g., Kraemer and Reid, 1984;  
360 Gonnee et al., 2008; Kiro et al., 2012; Vinson et al., 2013), and assuming a non-complete frozen nature of the  
permafrost (e.g., Gilbert et al., 2019; Keating et al., 2018; Weinstein et al., 2019). However, the observation that  
this is the case only with the short-lived isotopes, while not with the long-lived  $^{226}\text{Ra}$ , raises the possibility of a  
timing control on the radium isotopes of ground ice in this core (e.g., Weinstein et al., 2019, 2021), namely that  
the relatively low  $^{226}\text{Ra}$  (compared with  $^{223}\text{Ra}$ ) is due to a short residence time of the ADE-2 ground ice. Time  
365 constraints will be further discussed below.

Another important observation is that in ADE-2, both  $(^{226}\text{Ra}/^{223}\text{Ra})_{\text{AR}}$  and  $(^{226}\text{Ra}/^{224}\text{Ra})_{\text{AR}}$  activity ratios in ground  
ice are similar to (i.e., close to equilibrium with) their parent nuclide activity ratios ( $^{230}\text{Th}/^{227}\text{Ac}$  and  $^{230}\text{Th}/^{228}\text{Th}$ ,  
respectively) in the CEC sediment fraction (i.e., surface of grains). On the other hand, in ADE-17 radium ratios  
are consistently higher and are closer to parent ratios in the bulk sediment (Figs. 8a-b). We note that while Th and  
370 Ac isotope activities were measured only in the ADE-17 sediment, the very close proximity of the cores (within  
30 m) and the relatively uniform Th isotope ratios along the sediment profile (at least regarding the CEC, [Table  
C3](#)) suggest that the measured sediment nuclide ratios should not be very different between the ADE core locations.  
In fact,  $^{226}\text{Ra}$  activities in ground ice (1-60 dpm l<sup>-1</sup>) of all three cores are significantly lower than the  $^{230}\text{Th}$  in the  
CEC (0.02-0.17 dpm g<sup>-1</sup>, [Table C3](#)), which considering a dry solid density of 2.5 g/cc and a relatively high porosity  
375 of 50% (100% ice content, Table C1), is equivalent to 50-425 dpm l<sup>-1</sup> (Fig. 11; a more conservative porosity of  
25% will triplicate these activities). The lower than calculated activities are probably the result of most of recoiled  
radium being kept on grain surfaces (Fleischer and Raabe, 1978; Suksi and Rasilainen, 1996) or concentrated in  
liquid films attached to the grains. Notably, sample DR-AD-125, which is characterized by an exceptionally high



380 salinity (Cl<sup>-</sup> higher than seawater, Fig. 4, Table C1), showed unusually high radium activities of all isotopes (Table C2), probably due to lower radium adsorption onto grains.

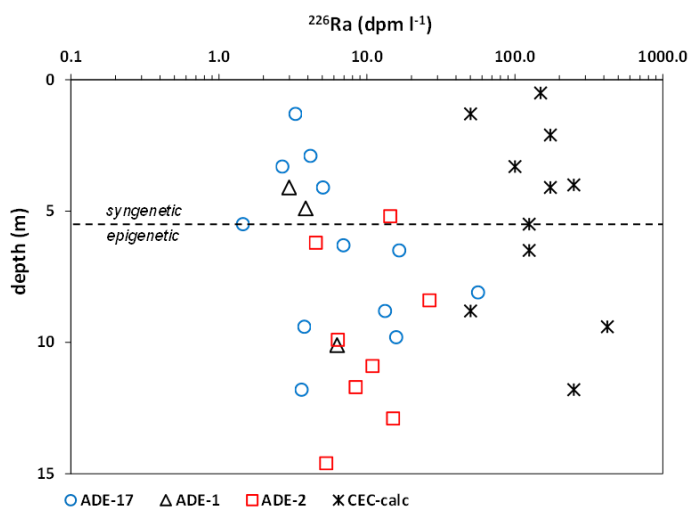


Figure 11: <sup>226</sup>Ra (dpm l<sup>-1</sup>) in ground ice of the three ADE cores and its calculated activities on CEC (CEC-calc) fraction. Note the logarithmic axis. The dashed line as in Figure 3.

### 5.2.1 Ground ice residence times

385 The similarity between (<sup>226</sup>Ra/<sup>87</sup>Ra)<sub>AR</sub> (sl = ‘short-lived’) ratios in ADE-2 and the <sup>230</sup>Th/parent nuclide activity ratios in the CEC fraction (Figs. 7 and 8) suggests that pore space radium isotopes are in equilibrium with parent nuclides on grain surfaces. Equilibrium ratios are supposed to be achieved within 5-6 half-lives of the longer-lived isotope (i.e., <sup>226</sup>Ra, with a half-life of 1600 years), or shorter if adsorption is involved (Kiro et al., 2013; Weinstein et al., 2021). The concentration of a certain Ra isotope in groundwater at time t is described by Equation (1),  
 390 assuming negligible dissolution and diffusion (e.g., Kiro et al., 2013; Weinstein et al., 2021), as is probably the case in the ground ice.

$$C = \frac{P}{\lambda(K+1)} (1 - \exp^{-\lambda(K+1)t}) + C_0 \exp^{-\lambda(K+1)t} \quad (1)$$

C is the activity [dpm l<sup>-1</sup>] of the isotope, C<sub>0</sub> is the initial activity [dpm l<sup>-1</sup>] (when the fluid/ice was emplaced in pore space), P is the production by recoil from the sediment [dpm l<sup>-1</sup> yr<sup>-1</sup>], λ is the decay constant of the isotope [yr<sup>-1</sup>]  
 395 and K is a unitless adsorption coefficient. The short-lived isotopes <sup>224</sup>Ra and <sup>223</sup>Ra reach steady state activities within weeks, which for the discussed time scales practically means a uniform activity. Accordingly, we will make use of the average isotope activity in ADE-2 e.g. 1.4 dpm l<sup>-1</sup> for <sup>223</sup>Ra (Table C2). Therefore, activity ratios of long to short-lived isotopes solely depend on the initial and the buildup of <sup>226</sup>Ra activities.

While C<sub>0</sub> of <sup>226</sup>Ra is not well-constrained for the shallow (syngenetic) layers, we may assume that the deeper, epigenetic layers had initial activities similar to that of typical shelf seawater (e.g., 0.1 dpm l<sup>-1</sup>, Moore, 1996). In  
 400 Fig. 12, we show the buildup of (<sup>226</sup>Ra/<sup>223</sup>Ra)<sub>AR</sub> in the ground ice with time. Assuming no adsorption (K=0 for a completely frozen pore space), (<sup>226</sup>Ra/<sup>223</sup>Ra)<sub>AR</sub> will reach CEC <sup>230</sup>Th/<sup>227</sup>Ac activity ratios (secular equilibrium)



within several thousands of years. We note that even if initial  $^{226}\text{Ra}$  activities is an order of magnitude higher, the time to reach equilibrium values would be similar (see Fig. 12). Times could shorten significantly if liquid is present in the pore space, as is sometimes the case in the studied area (e.g. Keating et al. 2018; Weinstein et al. 2019), thus allowing adsorption to take place. For instance, if  $K=10$ , as is the case for seawater salinities, (e.g., Weinstein et al., 2021; Garcia-Orellana et al., 2021), time to reach equilibrium will be on the order of 100's years. However, the cryotic conditions and the more common observation of a frozen pore space do not favor too much adsorption. Accordingly, while the Th- Ra secular equilibrium cannot be quantitatively used for residence time determination, it still indicates that the ground ice in ADE-2 has not been recently formed, and that it is probably at least 100's years old. The upper limit on the residence time in ADE-2 should be achieved by circumstantial observations, as follows.

As noted, and unlike ADE-2,  $(^{226}\text{Ra}/^{223}\text{Ra})_{\text{AR}}$  in ground ice of ADE-17 (and ADE-1) are significantly higher than the CEC parent nuclide ratios (e.g.,  $(^{226}\text{Ra}/^{223}\text{Ra})_{\text{AR}}$  is mostly 20 - 70), being much closer to (although not in equilibrium with) bulk sediment parent  $^{230}\text{Th}/^{227}\text{Ac}$  ratios (Fig. 8a). This suggests that on top of contribution from the CEC fraction, there was enough time in ADE-17 for some  $^{226}\text{Ra}$  to diffuse out of the mineral grains. On the other hand,  $^{223}\text{Ra}$ , with a half-life of 11 days, is not relevant for diffusion from inside the grains, therefore the high  $(^{226}\text{Ra}/^{223}\text{Ra})_{\text{AR}}$ .

Unfortunately, we have no good control on diffusion rates under cryotic conditions (see discussion in section 5.2.2), but the maximum time allowed for ground ice formation in the study site could be easily constrained. Valley-fill marine sediments at the ADE site are of Early Holocene age ( $\leq 10,500$  years, e.g., Lønne and Nemeč, 2004), and freezing occurred no earlier than 9.5 ka, after being exposed to the atmosphere due to the elastic rebound (e.g., Gilbert et al., 2018; Rotem et al., 2023). This means that ground ice is no older than Early Holocene,

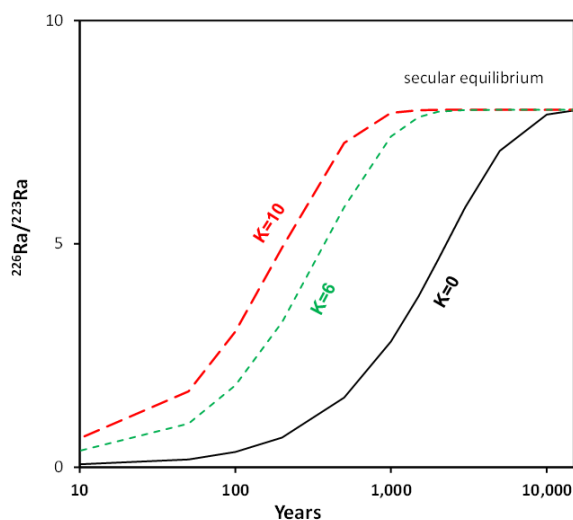


**Figure 12: Simulations of the buildup of  $(^{226}\text{Ra}/^{223}\text{Ra})_{\text{AR}}$  in permafrost pore space with different adsorption coefficients ( $K=0$  means no adsorption). See text for further explanations.**

and that 9-10 kyr has been enough time for a significant diffusion from inside the grains to occur in ADE-17. Moreover, high  $(^{226}\text{Ra}/^{223}\text{Ra})_{\text{AR}}$  are also found in the syngenetic (shallow) part of the permafrost profile (Fig. 7a),



430 which has been deposited between 4-2 kyr ago (Gilbert et al., 2018). This implies that even 4-2 thousand years are enough for a significant diffusion of  $^{226}\text{Ra}$  out of the grains (probably, from outer portions). As a matter of fact, only a small fraction of the produced  $^{226}\text{Ra}$  has to diffuse out of the grains in order to produce the high  $(^{226}\text{Ra}/^{232}\text{Th})_{\text{AR}}$ . With a bulk  $^{230}\text{Th}$  of 4-8 dpm/g (Table C3), a dry density of 2.5 g/cc, porosity of 25-50% (i.e., 50-100% ice content, Table C1) and 50% emanation (release to pore space),  $^{226}\text{Ra}$  in ground ice should be as high as 20,000-100,000 dpm/l, which is 3-4 orders higher than that observed in the ground ice (Table C2). Based on the observations in ADE-17 and its time scales, the consistently lower  $(^{226}\text{Ra}/^{232}\text{Th})_{\text{AR}}$  in the epigenetic ground ice of core ADE-2 constrains its residence time to  $\ll 2,000$  years (Fig. 13). The meaning of this short residence time is discussed in section 5.3.

435

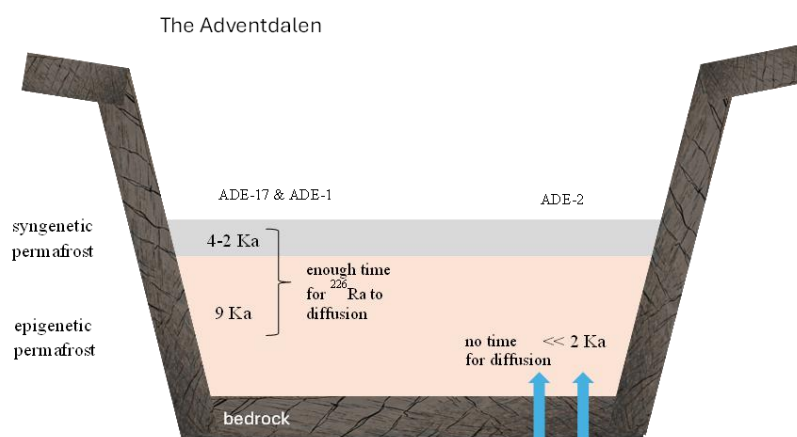


Figure 13. Conceptual model of the heterogeneous nature of ground ice in the Adventdalen study site.

#### 5.2.2 Diffusion from grains in the permafrost

440 Ramma and Moore (1984), showed experimentally that radon can diffuse out from sand grains within days, which was attributed to diffusion via nanopores. On the other hand, they argued that other, non-gaseous nuclides of the U-Th chains could not make it to the intergranular space, owing to adsorption in the nanopores. We believe that while radium diffusion could indeed be negligible in the short-term (days), it is not necessarily the case for the long term, i.e., 100's-1000's years. Moreover, adsorption is orders of magnitude lower in saline water and hardly exists when pore space is frozen. Since we deal with either completely or partially frozen saline ground ice, we believe that adsorption is less intense and that radium diffusion from inside the grains could be significant, when thousands of years are considered, in particular in grain size much smaller (silt and clay) than in the mentioned experiments (sand).

445 To the best of our knowledge, there is no data for low-T diffusion in solids, and there is hardly any data for sub-zero diffusion. Nevertheless, extrapolation from higher temperature data (e.g., for Ca) predicts D's (diffusion coefficients) in solids on the order of  $\ll 10^{-24} \text{ m}^2 \text{ sec}^{-1}$  (e.g., Brady and Cherniak, 2010; Cherniak, 2010), which does not take into account the nanopore pathway. On the other hand, there is some data for diffusion of molecules



(no single cations) in ice under a much lower than permafrost temperature (i.e., 100-140 °K), which is about  $10^{-16}$   $\text{m}^2\text{cm}^{-1}$  (e.g., Ghesquière et al., 2015). The effective diffusion coefficient in the permafrost soil grains should be dependent on the concentration of nano-pores, the cryotic condition of the fluid in the nano-pores and porosity. In

455 Fig. 14, we arbitrarily used effective diffusion coefficients of  $10^{-23}$ - $10^{-24}$   $\text{m}^2 \text{sec}^{-1}$  and distances relevant to clay minerals (0.5-2  $\mu\text{m}$ ) just in order to show that there could be a significant difference (up to one order of magnitude) in  $^{226}\text{Ra}$  activities between Early and Late Holocene ground ice. Simulations were performed using the following equation:  $Ra_p/Ra_g = \text{erfc}\left\{\frac{x}{2\sqrt{De\frac{t}{pR}}}\right\}$ , where  $Ra_p/Ra_g$  = activity in pore space relative to that in the grain,

$x$ =effective distance [m],  $De$ =effective diffusion coefficient [ $\text{m}^2 \text{sec}^{-1}$ ],  $t$ =time [sec],  $p$ =porosity [unitless],

460  $R$ =retardation factor [ $=K+1$ , unitless, Krishnaswami et al., 1982].  $R$  was assumed 10 for saline water.

We stress that the diffusion coefficients used for this figure are not based on any empirical data, and they were used only to show that diffusion could affect the long-lived  $^{226}\text{Ra}$ . Slower diffusion rates (lower  $D$ 's) could still be effective with smaller diffusion distances (i.e., from grain rims,  $\ll 1\mu\text{m}$ ). Fig. 14 also shows that diffusion is strongly dependent on porosity. Another factor that affects diffusion is the retardation (i.e. adsorption), which is

465 highly dependent on the existence of liquid, as well as on its salinity, redox, and pH conditions. In general, the higher the  $R$ , the lower the effective diffusion is. In Fig. 14, we used  $R=10$ , which is for nanopores filled with saline water (e.g., Weinstein et al., 2021; Garcia-Orellana et al., 2021). However, with nanopores being mostly or completely frozen, the effect of adsorption is minimized, therefore  $R$  should be low even with fresh water.

To summarize this part, while we do not have low- $T$  diffusion data, and while the effective diffusion is highly

470 dependent on sediment texture and cryotic conditions, we do suggest that pore space  $^{226}\text{Ra}$ , thereby  $(^{226}\text{Ra}/^{223}\text{Ra})_{AR}$ , is highly dependent on diffusion from grains, reflecting on ground ice residence time.

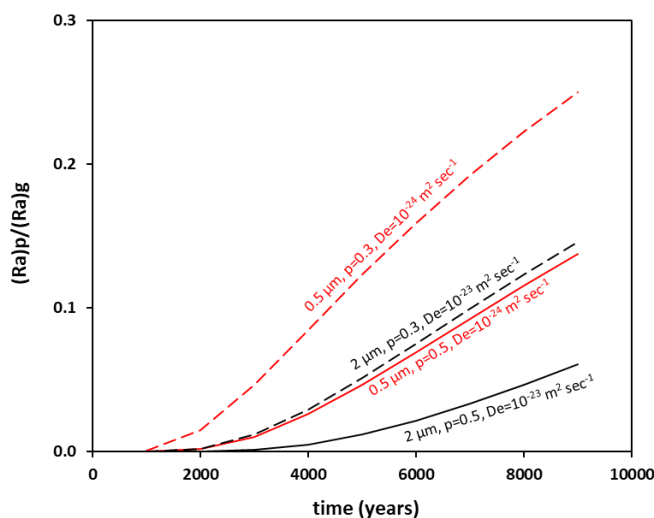


Figure 14: Simulations of diffusion from sediment clay grains into the pore space. See text for the diffusion coefficients used. Solid and dashed lines are for high and low porosity (0.5 and 0.3, respectively). See text for explanation about the simulations.



475 **5.3. Sources of ground ice and permafrost dynamics**

The co-existence of pore fluids (ground ice) with different chemical composition and supposedly distinct history (residence time) at the same site and depth (from the surface), and the comprehension that the ground ice along the profile of one of the cores (ADE-2) is relatively young, calls for dynamic visualization of the permafrost at Adventdalen. Rotem et al., (2023) suggested that the saline water found at the top of the epigenetic section in  
480 ADE-17, at >10 m.a.s.l, has been preserved due to the immediate formation of permafrost following seawater regression from this site, ca. 9 ka. It is also apparent that some of the water went through water:rock interaction while in the sediment, probably prior to freezing (e.g., high Na/Cl and SO<sub>4</sub>/Cl, Fig. 5), possibly when still covered with seawater.

Accordingly, the similar to seawater composition of the ground ice at ADE-2 and its implied short (<2000 yrs)  
485 residence time, as suggested by the (<sup>226</sup>Ra/<sup>238</sup>Ra)<sub>AR</sub>, is quite enigmatic. A direct active connection to the nearby fjord, the Adventfjorden (Fig. 1) via sub-permafrost groundwater flow (i.e., seawater circulation) is unlikely because of the distance from the fjord (~10 km) and the depth it should gain following a Ghyben-Herzberg approximation (i.e., assuming a hydrostatic head close to the surface elevation of 23 m.a.s.l. and common seawater salinity, then the fresh-saline water interface should be at ca. 800-900 m depth; lower fjord water salinity should  
490 result in even deeper interface). Moreover, considering the basement geology (shales underlain by sandstones, e.g., Ogata et al., 2014) and the low hydraulic gradients involved (ca. 2‰, assuming it is parallel to the topographic gradient), the flow rate should not be much more than 1 m y<sup>-1</sup> (e.g., Hornum et al., 2020), which would result in residence times of several thousand years at the study site, in discordance with the implied young age. Thus, it seems that the low (<sup>226</sup>Ra/<sup>238</sup>Ra)<sub>AR</sub> at ADE-2 is the result of a Ra clock reset ('apparent' residence time) rather than  
495 due to actual residence time in the aquifer.

The buildup of radium isotope activity in the pore space, whether hosting water or ground ice, depends on several factors, including (1) the mineralogy of aquifer solids, (2) grain size and (3) pore space:solid ratio. The migration of water from Th-poor to a Th-rich lithology, as well as from high water:rock to low water:rock ratio environment, should result in an increased supply of radium, therefore possibly in the reset (or a partial reset) of the Ra isotope-ratio clock. Impact on radium release and resultant reset will be even stronger, if the intruding water is more saline than the older one (assuming a non-completely frozen environment), therefore reducing the adsorption effect. Accordingly, it is suggested that the ground ice in ADE-2 recently experienced a local intrusion of water, which previously resided in a low-Th or a high water:rock ratio aquifer. Such an aquifer could be the Early Cretaceous sandstone Helvetiafjellet Formation, which is located >70 m beneath the surface at the site (ca. 60 m below the  
500 Adventdalen sediment fill, e.g., Ogata et al., 2014), although the possibility of a deeper source (e.g., the Triassic to Early Jurassic fractured sandstone Geerdalen Formation; Mulrooney et al., 2018) could not be excluded. Sandstone, in particular fractured, usually has a high water:rock ratio, as well as a low thorium content, compared with the silt-dominated sediments that comprise the valley infill. Sandstone could also explain the limited water-rock interaction, which is demonstrated by the similarity to seawater composition in the ADE-2 ground ice (Fig.  
510 4). Logs taken at deep boreholes in Adventdalen, albeit closer (5 km) to the sea, indicated that groundwater salinity in the Helvetiafjellet Formation (and deeper) is ≥20 mS/cm (~40% seawater conductivity; Braathen et al., 2012), which could also be the case in the basement rocks beneath ADE.



The ascent of water from the sub-permafrost zone is demonstrated in Svalbard by artesian discharge, associated with the common pingo structures (e.g., Demidov et al., 2019; Hodson et al., 2020; Rotem et al., 2024). This discharge is controlled either by hydraulic heads from the surrounding mountains or by basal permafrost aggradation (e.g., Hornum et al., 2020). Intra-permafrost intrusion or segregation events were also documented in various environments (e.g., French, 2007; Weinstein et al., 2019), sometimes related to non-frozen cryopeg lenses (e.g., Stephani et al., 2020; Iwahana et al., 2021). Although not a massive ice body, like in the common segregated and intrusive ice (e.g., Humlum et al., 2003; Demidov et al., 2021), it is proposed that the relatively ‘young’ (<2000 years) ground ice of ADE-2 was formed by saline fluids that arrived from the underlying sandstone reservoir (Fig. 13), possibly forced by the same hydraulic pressure that drives artesian discharge in the nearby pingos (e.g., Hornum et al., 2020). These fluids have been emplaced (intruded) in the shallower permafrost zone in a fingering style, which resulted in the local heterogeneity at the ADE site.

We note that since ground ice analysis has been performed on large core segments (length >0.5 m) and considering the very variable salinity (e.g., 2,000 to >20,000 mgCl l<sup>-1</sup> in the epigenetic zone, depth of 5-15 m from the surface, Fig. 3a), we do not have a good resolution of the saline ground ice distribution. Accordingly, it could as well be that the high salinity observed is in fact due to small pockets of higher salinity, where the fingering intrusive fluids managed to intrude pore space. We also have no indication of the intrusion pathways, which should be further studied.

530

#### 5.4 The <sup>224</sup>Ra/<sup>228</sup>Ra enigma

The relatively low daughter-parent <sup>224</sup>Ra/<sup>228</sup>Ra ratios (<<1) in permafrost ground ice have been noticed in several cases (Weinstein et al., (2019, in Svalbard, Kipp et al., (2025) in Arctic Canada, and Zhang et al., (2025) worldwide). This is remarkably different from the common steady state ratios of 1-2, mentioned in most groundwater publications (e.g., Krishnaswami et al., 1982; Davidson and Dickson, 1986; Kiro et al., 2015). Interestingly, low ratios also appear in deep, old brines from coastal Israel (Weinstein et al., 2021). In both cases, this was attributed to the adsorption of <sup>228</sup>Th (direct <sup>224</sup>Ra parent, <sup>228</sup>Ra daughter) onto grain surfaces or aquifer rocks, thereby retaining some of the produced <sup>224</sup>Ra on the grains and preventing it from reaching the pore space fluid/ice. This, in turn, required the presence of some non-frozen fluid in the pore space, which is in agreement with the observed partially frozen nature of the permafrost in Svalbard and elsewhere (e.g., Keating et al., 2018; Weinstein et al., 2019).

Nevertheless, the results of this study (Fig. 9) suggest that this is not an across-the-board observation, and that some of the samples show ratios within the ‘expected’ range of 1-2. This is in particular observed in the deep, epigenetic samples of ADE-2. Considering the much lower half-lives involved (5.75 years for <sup>228</sup>Ra, days for <sup>224</sup>Ra), the difference in age between the cores does not seem relevant to the <sup>224</sup>Ra/<sup>228</sup>Ra ratios. On the other hand, it could have to do with the higher salinity in ADE-2, which could result in less adsorption of <sup>228</sup>Th and should be further studied.

#### 6. Summary and Conclusions

In this paper, we used Ra and Th isotopes to get an insight into the intra-permafrost ground ice history and fluid migration in the continuous permafrost of a Svalbard valley. While the dominant control on the contribution of short-lived Ra isotopes is the recoil of Th-parent nuclides residing on the soil grain surfaces, the supply of the



long-lived  $^{226}\text{Ra}$  is also controlled by slow diffusion out of the soil grains. These are superimposed by adsorption, which is related to the common presence of fluid in the cryotic pore space of the saline permafrost, and which  
555 affects similarly both radium isotope activities and the time of reaching secular equilibrium. The relatively low  
( $^{226}\text{Ra}/^{230}\text{Th}$ )<sub>AR</sub> in one core (ADE-2) and its equilibrium with grain surface ratios of thorium isotope parents, while  
much higher Ra isotope ratios in the other two core (ADE-17 and ADE-1), suggest that ground ice in the first is  
younger, probably related to recent fluid intrusion and Ra isotope clock reset. The similarity to seawater  
composition in this young ground ice suggests that the intruding fluids were less subjected to WRI, which is  
560 probably due to the characteristic higher water:rock ratio of its source aquifer, most likely the local basement. On  
the other hand, the different from seawater composition in the other two cores suggests that the water had a  
significantly longer history in the valley-fill sediments prior to freezing, which is in accordance with their  
suggested longer residence time.

This study demonstrates the heterogeneity of saline permafrost and highlights its complex history and liability to  
565 fluid migration, which is probably also the case in other permafrost terrains. This further highlights saline  
permafrost's vulnerability to the ongoing climate change and warming.



**Appendices**

**570 Tables C1, C2 and C3**

**Table C1. Inorganic ion concentrations and ice content\* of ground ice in the ADE cores, East Adventdalen**

Sample	permafrost type	depth	Cl <sup>-</sup>	Br <sup>-</sup>	SO <sub>4</sub> <sup>-</sup>	SiO <sub>2</sub>	Na <sup>+</sup>	K <sup>+</sup>	Sr <sup>++</sup>	Ca <sup>++</sup>	Mg <sup>++</sup>	HCO <sub>3</sub> <sup>-</sup>	ice content
ADE-17		M	mg l <sup>-1</sup>	mg l <sup>-1</sup>	mg l <sup>-1</sup>	mg l <sup>-1</sup>	mg l <sup>-1</sup>	mg l <sup>-1</sup>	mg l <sup>-1</sup>	mg l <sup>-1</sup>	mg l <sup>-1</sup>	mg l <sup>-1</sup>	%
DR-AD-55	Syngenetic	1.3	27.3	0.5	23.5	12.8	11.3	18.1	0.20	5.5	15.5	---	165
DR-AD-58	Syngenetic	2.1	12.7	0.6	29.7	14.0	19.7	3.8	0.41	8.8	27.8	---	69
DR-AD-52	Syngenetic	2.9	72.1	0.7	24.1	8.8	15.5	46.9	0.61	12.6	35.3	---	88
DR-AD-57	Syngenetic	3.3	14.0	0.5	29.1	5.9	32.6	4.8	0.13	3.6	7.7	---	170
DR-AD-56	Syngenetic	3.5	9.9	0.3	11.8	5.3	13.2	4.4	0.07	1.5	2.6	---	149
DR-AD-61	Syngenetic	4.0	14.5	0.7	13.0	11.6	9.5	5.2	0.16	3.6	8.8	---	100
DR-AD-63	Syngenetic	4.1	26.8	---	13.4	29.8	13.0	14.1	0.13	1.7	2.8	---	131
DR-AD-59	Syngenetic	5.5	65.3	0.6	156.5	19.9	81.2	20.6	0.51	13.5	27.8	---	105
DR-AD-53	Epigenetic	6.3	468.3	2.1	102.4	20.5	449.9	0.7	0.53	14.5	3.6	---	14
DR-AD-64	Epigenetic	6.5	765.3	---	362.5	34.7	750.3	29.1	0.15	11.5	---	---	27
DR-AD-65	Epigenetic	8.1	1491.1	---	446.3	19.3	1154.4	35.6	0.08	1.7	---	---	22
DR-AD-54	Epigenetic	9.4	1896.9	7.0	483.7	8.5	2209.7	181.9	0.30	16.3	---	---	21
DR-AD-66	Epigenetic	9.8	3229.6	---	704.6	23.2	2498.3	45.8	0.34	9.7	---	---	10
DR-AD-60	Epigenetic	11.8	2246.3	6.6	400.5	19.4	2161.1	97.1	0.53	17.8	---	---	14
ADE-1													
DR-AD-146	Syngenetic	4.1	20.0	---	34.8	6.0	17.0	2.9	0.15	7.0	3.1	9.0	182
DR-AD-147	Syngenetic	4.9	---	0.8	139.8	12.9	84.4	13.7	0.67	36.6	17.4	35.1	87
DR-AD-128	Epigenetic	5.7	445.0	1.9	41.8	8.0	270.0	23.6	0.37	21.6	16.4	85.1	35
DR-AD-129	Epigenetic	6.1	902.0	3.7	176.0	10.2	626.0	57.1	0.45	25.5	25.0	232.1	22
DR-AD-130	Epigenetic	6.4	1157.3	4.2	261.5	10.1	866.9	50.1	0.21	10.5	16.4	197.6	45
DR-AD-131	Epigenetic	6.9	1226.4	4.3	468.6	9.6	1012.7	42.4	0.16	7.7	10.9	143.6	27
DR-AD-149	Epigenetic	7.9	2348.7	5.6	1418.0	4.0	2043.6	98.2	0.51	19.4	30.6	227.2	17
DR-AD-123	Epigenetic	10.1	1275.6	4.0	200.3	9.6	961.3	8.8	0.04	0.7	---	183.9	16
DR-AD-148	Epigenetic	11.0	1718.7	4.2	978.9	7.7	1434.4	90.8	0.50	18.5	24.6	195.2	29
ADE-2													
DR-AD-145	Syngenetic	5.2	5010.0	119.1	1548.8	8.6	3259.8	241.5	2.57	122.6	176.3	243.0	23
DR-AD-126	Epigenetic	6.2	5035.7	17.3	465.9	9.3	3209.7	152.8	1.45	61.8	128.9	151.0	23
DR-AD-132	Epigenetic	7.6	7079.1	24.6	445.7	7.6	4240.9	223.3	2.85	102.4	234.2	45.9	13
DR-AD-125	Epigenetic	8.4	23194.9	78.9	801.9	20.6	14624.5	367.0	6.03	222.2	366.6	611.9	2
DR-AD-124	Epigenetic	9.9	4616.5	15.8	573.7	7.8	3041.5	156.1	1.69	62.4	110.5	164.5	45
DR-AD-150	Epigenetic	10.9	6521.9	17.6	2094.9	29.3	3928.9	2487.8	---	1.4	7.9	340.4	13
DR-AD-122	Epigenetic	11.7	5420.0	17.8	631.5	11.5	3552.7	160.2	2.29	85.2	115.2	239.3	12
DR-AD-133	Epigenetic	12.3	7071.5	26.0	724.5	7.2	4129.4	215.9	4.50	164.3	268.5	66.7	116
DR-AD-151	Epigenetic	12.9	7961.7	22.0	2729.2	7.3	5329.8	377.7	6.61	240.8	292.6	222.5	20
DR-AD-134	Epigenetic	13.9	2774.2	8.2	266.9	6.3	1505.5	75.8	2.57	77.2	106.7	---	13
DR-AD-121	Epigenetic	14.6	4474.1	14.5	333.9	9.9	2679.3	107.9	4.07	91.3	106.1	191.3	25

\*ice content = ice/dry weight



575 **Table C2.** Radium isotope activities\* and ratios in ground ice, ADE cores.

sample	permafrost type	depth	<sup>223</sup> Ra	<sup>224</sup> Ra	<sup>226</sup> Ra	<sup>228</sup> Ra	<sup>226</sup> Ra/ <sup>223</sup> Ra	<sup>226</sup> Ra/ <sup>224</sup> Ra	<sup>226</sup> Ra/ <sup>228</sup> Ra	<sup>224</sup> Ra/ <sup>228</sup> Ra
		m	dpm l <sup>-1</sup>	dpm l <sup>-1</sup>	dpm l <sup>-1</sup>	dpm l <sup>-1</sup>				
ADE-17										
DR-AD-55	Syngenetic	1.3	0.07	1.46	3.26	9.53	44.7	2.2	0.3	0.15
DR-AD-58	Syngenetic	2.1	---	---	---	---	125.0	---	---	---
DR-AD-52	Syngenetic	2.9	0.18	2.16	4.13	10.11	23.3	1.9	0.4	0.21
DR-AD-57	Syngenetic	3.3	0.02	0.13	2.71	0.99	122.0	20.3	2.7	0.13
DR-AD-56	Syngenetic	3.5	---	---	---	---	58.2	---	---	---
DR-AD-61	Syngenetic	4.0	---	---	---	---	24.0	---	---	---
DR-AD-63	Syngenetic	4.1	0.11	1.89	5.01	3.04	43.6	2.6	1.6	0.62
DR-AD-59	Syngenetic	5.5	0.06	0.50	1.44	9.00	25.7	2.9	0.2	0.06
DR-AD-53	Epigenetic	6.3	0.21	5.02	6.90	7.41	33.0	1.4	0.9	0.68
DR-AD-64	Epigenetic	6.5	0.23	2.13	16.54	16.71	72.2	7.8	1.0	0.13
DR-AD-65	Epigenetic	8.1	1.02	12.88	56.49	20.44	55.4	4.4	2.8	0.63
DR-AD-67	Epigenetic	8.8	0.32	7.04	13.24	---	41.6	1.9	---	---
DR-AD-54	Epigenetic	9.4	0.23	3.10	3.74	16.67	16.0	1.2	0.2	0.19
DR-AD-66	Epigenetic	9.8	0.27	3.83	15.78	18.88	57.7	4.1	0.8	0.20
DR-AD-60	Epigenetic	11.8	0.20	2.60	3.60	27.56	18.0	1.4	0.1	0.09
ADE-1										
DR-AD-146	Syngenetic	4.1	0.03	0.59	2.96	---	109.2	5.0	---	---
DR-AD-147	Syngenetic	4.9	0.10	0.85	3.87	---	39.0	4.5	---	---
DR-AD-149	Epigenetic	7.9	---	---	---	---	14.7	---	---	---
DR-AD-123	Epigenetic	10.1	0.19	2.12	6.26	---	32.5	3.0	---	---
DR-AD-148	Epigenetic	11.0	---	---	---	---	14.4	---	---	---
ADE-2										
DR-AD-145	Syngenetic	5.2	1.03	18.95	14.47	---	14.1	0.8	---	---
DR-AD-126	Epigenetic	6.2	0.64	8.44	4.49	15.28	7.0	0.5	0.3	0.55
DR-AD-125	Epigenetic	8.4	1.87	27.57	26.56	25.50	14.2	1.0	1.0	1.08
DR-AD-124	Epigenetic	9.9	0.86	8.81	6.36	14.84	7.4	0.7	0.4	0.59
DR-AD-150	Epigenetic	10.9	1.45	24.64	10.95	---	7.6	0.4	---	---
DR-AD-122	Epigenetic	11.7	0.76	10.83	8.39	6.84	11.0	0.8	1.2	1.58
DR-AD-151	Epigenetic	12.9	3.92	58.66	14.99	---	3.8	0.3	---	---
DR-AD-121	Epigenetic	14.6	0.94	18.24	5.32	12.16	5.7	0.3	0.4	1.50

\*Activities are not presented for samples with Ra adsorption efficiencies lower than 50%.



**Table C3.** Thorium isotopes activities and <sup>227</sup>Ac in sediments from ADE-17

sample	permafrost type	depth m	<sup>232</sup> Th	<sup>230</sup> Th	<sup>228</sup> Th	<sup>227</sup> Ac	<sup>232</sup> Th	<sup>230</sup> Th	<sup>228</sup> Th	<sup>227</sup> Ac	<sup>230</sup> Th/ <sup>227</sup> Ac	<sup>230</sup> Th/ <sup>227</sup> Ac	<sup>230</sup> Th/ <sup>228</sup> Th	<sup>230</sup> Th/ <sup>228</sup> Th	<sup>230</sup> Th/ <sup>232</sup> Th	<sup>230</sup> Th/ <sup>232</sup> Th	CEC
			dpm g <sup>-1</sup>	bulk	CEC	bulk	CEC	bulk	CEC								
DR-AD-51	Active layer	0.5	5.3	4.5	0.7	0.02	0.12	0.06	0.28	0.02	267	3.4	6.4	0.22	0.86	0.53	
DR-AD-55	Syngenetic	1.3	5.5	4.3	1.0	0.06	0.03	0.02	0.08	0.01	79	2.6	4.4	0.23	0.79	0.69	
DR-AD-58	Syngenetic	2.1	6.8	4.7	0.9	0.08	0.13	0.07	0.14	---	62	---	5.5	0.51	0.70	0.55	
DR-AD-57	Syngenetic	3.3	6.8	5.2	0.6	0.07	0.06	0.04	0.15	0.01	78	6.2	9.2	0.25	0.76	0.60	
DR-AD-61	Syngenetic	4.0	6.4	5.3	0.4	0.03	0.17	0.10	0.23	---	191	---	12.4	0.43	0.83	0.57	
DR-AD-63	Syngenetic	4.1	6.3	5.2	0.6	0.07	0.11	0.07	1.20	0.01	71	7.7	9.0	0.06	0.83	0.61	
DR-AD-59	Syngenetic	5.5	4.9	5.0	0.5	0.06	0.07	0.05	0.45	---	83	---	10.1	0.11	1.02	0.75	
DR-AD-64	Epigenetic	6.5	7.9	7.6	0.3	---	0.04	0.05	0.10	0.01	---	5.2	24.4	0.54	0.95	1.33	
DR-AD-67	Epigenetic	8.8	7.8	7.1	0.4	0.07	0.01	0.02	0.61	0.01	100	1.9	19.2	0.03	0.91	1.75	
DR-AD-54	Epigenetic	9.4	8.4	7.0	0.7	0.04	0.10	0.17	0.29	0.02	185	8.5	9.8	0.58	0.84	1.69	
DR-AD-60	Epigenetic	11.8	5.9	5.9	0.4	0.02	0.06	0.10	0.27	0.02	371	4.9	15.6	0.38	1.00	1.61	



#### Data availability

580 Data is available through DOI: [10.6084/m9.figshare.30959015](https://doi.org/10.6084/m9.figshare.30959015)

#### Author contribution

DR, YW, and HHC planned the drilling campaigns; DR and YW processed the cores and lab work in UNIS Svalbard; DR and YH performed the water and soil fractions chemistry analysis at GSI; AT performed soil fraction  
585 analyses at the Hebrew University lab. YW developed the simulations of radium isotopes diffusion from sediment clay grains into the pore space; DR and YW wrote the manuscript. All authors commented on the manuscript.

#### Competing interests

The authors declare that they have no conflict of interest.

590

#### Acknowledgments

We would like to express our gratitude to Ullrich (Ulli) Neuman for leading the 2017 and 2022 drilling campaigns in Adventdalen. Many thanks to Andreas Alexander and Graham L. Gilbert for field assistance, to Danni Rohdent and Mai-Brit Schulte for assistance in the lab, and to Gerd-Irene Sigernes and the UNIS logistics personnel for  
595 their great assistance with field and laboratory gear. We are also very thankful to the GSI researchers and technicians Olga Berlin, Galit Sharabi, Dina Shitber, Keren Weiss, and Anton Vaks, who helped with chemical and Th isotope analysis.

#### Financial support

600 The project was funded by the Israel Science Foundation grant ISF163/19, while the drilling campaigns were also supported by an Arctic Field Grant from the Norwegian Research Council, Project Number: 269988 RiS ID: 10664.

#### References

- 605 Abramov, A., Vishnivetskaya, T., and Rivkina, E.: Are permafrost microorganisms as old as permafrost? *FEMS Microbiol. Ecol.*, 97(2). <https://doi.org/10.1093/femsec/fiaa260>, 2021.
- Ahonen, L.: Permafrost: occurrence and physiochemical processes (POSIVA--01-05). POSIVA OY, Finland, 2001.
- Åkerman, H. J., and Malmström, B.: Permafrost Mounds in the Abisko Area, Northern Sweden. *Geografiska Annaler: Series A, Physical Geography*, 68(3), 155–165. <https://doi.org/10.1080/04353676.1986.11880169>, 1986.
- 610 Alekseyev, V.R.: Cryogenesis and geodynamics of icing valleys. *Geodyn. Tectonophys.* 6 (2), 171–224. <https://doi.org/10.5800/GT-2015-6-2-0177>, 2015.
- Anisimov, O. A., and Nelson, F. E.: Permafrost zonation and climate change in the northern hemisphere: results from transient general circulation models. *Clim. Change*, 35(2), 241–258. <https://doi.org/10.1023/A:1005315409698>, 1986.
- 615 Banin, A., and Anderson, D. M.: Effects of Salt Concentration Changes During Freezing on the Unfrozen Water Content of Porous Materials. *Water Resour. Res.*, 10(1), 124–128. <https://doi.org/10.1029/WR010i001p00124>, 1974.



- Boike, J., Roth, K., and Overduin, P. P.: Thermal and hydrologic dynamics of the active layer at a continuous permafrost site (Taymyr Peninsula, Siberia). *Water Resour. Res.*, 34(3), 355-363. <https://doi.org/10.1029/97WR03498>, 1998.
- Braathen, A., Bælum, K., Christiansen, H.H., et al.: The Longyearbyen CO<sub>2</sub> Lab of Svalbard, Norway—initial assessment of the geological conditions for CO<sub>2</sub> sequestration. *Nor. J. Geol.*, Vol 92, pp. 353–376. Trondheim 2012, ISSN 029-196X, 2012.
- 625 Brady, J. B., and Cherniak, D. J.: Diffusion in Minerals: An Overview of Published Experimental Diffusion Data. *Rev. Mineral. Geochem.*, 72, 899–920. <https://doi.org/10.2138/rmg.2010.72.20>, 2010.
- Brigham-Grette, J., and Hopkins, D. M.: Emergent Marine Record and Paleoclimate of the Last Interglaciation along the Northwest Alaskan Coast. *Quat. Res.*, 43(2), 159-173, 1995.
- Brouchkov, A.: Nature and distribution of frozen saline sediments on the Russian Arctic coast. *Permafr. Periglac. Process*, 13, 83–90. <https://doi.org/10.1006/qres.1995.1017>, 2002.
- 630 Brown, J., O. Ferrians, J. A. Heginbottom, E., and Melnikov, E.S.: Circum-Arctic Map of Permafrost and Ground-Ice Conditions, Version 2 [Data Set]. Boulder, Colorado, USA. National Snow and Ice Data Center, 2002.
- Cable, S., Elberling, B., and Kroon, A.: Holocene permafrost history and cryostratigraphy in the High-Arctic Adventdalen Valley, central Svalbard. *Boreas*, 47(2), 423-442. <https://doi.org/10.1111/bor.12286>, 2018.
- 635 Cherniak, D.J.: Cation Diffusion in Feldspars. *Reviews in Mineralogy & Geochemistry* 72, 691-733. DOI: 10.2138/rmg.2010.72.15, 2010.
- Christiansen, H. H., French, H. M., and Humlum, O.: Permafrost in the Gruve-7 mine, Adventdalen, Svalbard. *Norw. J. Geol.*, 59(2), 109–115. <https://doi.org/10.1080/00291950510020592>, 2005.
- Dafflon, B., Hubbard, S., Ulrich, C., Peterson, J., Wu, Y., Wainwright, H., and Kneafsey, T. J.: Geophysical estimation of shallow permafrost distribution and properties in an ice-wedge polygon-dominated Arctic tundra region. *Geophys.*, 81(1). <https://doi.org/10.1190/geo2015-0175.1>, 2016.
- 640 Davidson, M.R., and Dickson, B.L.: A porous flow model for steady state transport of radium in groundwater. *Water Resour. Res.* 22 (1), 34–44, 1986.
- de Baar, H.J.W., van Heuven, S.M.A.C., and Middag, R.: Ocean Salinity, Major Elements, and Thermohaline Circulation. In: White, W. (eds) *Encyclopedia of Geochemistry*. *Encyclopedia of Earth Sciences Series*. Springer, Cham, 2017.
- Demidov, N., Wetterich, S., Verkulich, S., Ekaykin, A., Meyer, H., Anisimov, M., Schirrmeister, L., Demidov, V., and Hodson, A. J.: Geochemical signatures of pingo ice and its origin in Grøndalen, west Spitsbergen. *The Cryosphere*, 13, 3155–316. <https://doi.org/10.5194/tc-13-3155-2019>, 2019.
- 650 Demidov, V., Wetterich, S., Demidov, N., Schirrmeister, L., Verkulich, S., Koshurnikov, A., Gagarin, V., Ekaykin, A., Terekchov, A., Veres, A., and Kozachek, A.: Pingo drilling reveals sodium–chloride-dominated massive ice in Grøndalen, Spitsbergen. *Permafr. Periglac. Process*, 32(4), 572-586. <https://doi.org/10.1002/ppp.2124>, 2021.
- Dickinson, W.W., and Rosen, M.R.: Antarctic permafrost: An analogue for water and diagenetic minerals on Mars. *Geology* 31 (3): 199–202. [https://doi.org/10.1130/0091-7613\(2003\)031<0199:APAAFV>2.0.CO;2](https://doi.org/10.1130/0091-7613(2003)031<0199:APAAFV>2.0.CO;2), 2003.
- 655 Dobinski, W.: Permafrost. *Earth Sci. Rev.*, 108(3-4), 158-169. <https://doi.org/10.1016/j.earscirev.2011.06.007>, 2011.



- Elverhøi, A., Svendsen, J. I., Solheim, A., Andersen, E. S., Milliman, J., Mangerud, J., and Hooke, R. L.: Late Quaternary Sediment Yield from the High Arctic Svalbard Area. *J. Geol.* 103(1). <https://doi.org/10.1086/629718>, 1994.
- 660 Ewing, S.A., Paces, J.B., O'Donnell, J.A., Jorgenson, M.T., Kanevskiy, M.Z., Aiken, G.R., Shur, Y., Harden, J.W., and Striegl, R.: Uranium isotopes and dissolved organic carbon in loess permafrost: modeling the age of ancient ice. *Geochim. Cosmochim. Acta* 152, 143–165. <https://doi.org/10.1016/j.gca.2014.11.008>, 2015.
- Fisher, D. A., Lacelle, D., and Pollard, W.: A model of unfrozen water content and its transport in icy permafrost soils: Effects on ground ice content and permafrost stability. *Permafr. Periglac. Process*, 31(1), 184–199. <https://doi.org/10.1002/ppp.2031>, 2019.
- 665 Fleischer, R. L., and Raabe, O.: Recoiling alpha-emitting nuclei. Mechanisms for uranium-series disequilibrium. *Geoch. Cosm. Act.*, 42(7), 973–978. [https://doi.org/10.1016/0016-7037\(78\)90286-7](https://doi.org/10.1016/0016-7037(78)90286-7), 1978.
- Forman, S. L., Lubinski, D. J., Ingólfsson, Ó., Zeeberg, J. J., Snyder, J. A., Siegert, M. J., and Matisov, G. G.: A review of postglacial emergence on Svalbard, Franz Josef Land and Novaya Zemlya, northern Eurasia. *Quat. Sci. Rev.*, 23(11–13), 1391–1434. <https://doi.org/10.1016/j.quascirev.2003.12.007>, 2004.
- 670 French H.: *The Periglacial Environment*. Copyright © 2007 by John Wiley & Sons, Ltd., 2007.
- French, H.: Recent contributions to the study of past permafrost. *Permafr. Periglac. Process*, 19(2), 179–194. <https://doi.org/10.1002/ppp.614>, 2008.
- Fu, Z., Wu, Q., Zhang, W., He, H., and Wang, L.: Water Migration and Segregated Ice Formation in Frozen Ground: Current Advances and Future Perspectives. *Front. Earth Sci.*, 10, 826961. <https://doi.org/10.3389/feart.2022.826961>, 2022.
- 675 Gao, Z., Lin, Z., Niu, F., Luo, J., Liu, M., and Yin, G.: Hydrochemistry and controlling mechanism of lakes in permafrost regions along the Qinghai-Tibet Engineering Corridor, China. *Geomorphology*, 297, 159–169. <https://doi.org/10.1016/j.geomorph.2017.09.020>, 2017.
- 680 Garcia-Orellana, J., Rodellas, V., Tamborski, J., Diego-Feliu, M., Van Beek, P., Weinstein, Y., Charette, M., Alorda-Kleinglass, A., Michael, H., Stieglitz, T., and Scholten, J.: Radium isotopes as submarine groundwater discharge (SGD) tracers: Review and recommendations. *Earth Sci. Rev.*, 220, 103681. <https://doi.org/10.1016/j.earscirev.2021.103681>, 2021.
- Ghesquière, P., Mineva, T., Talbi, D., Theulè, P., Noble, J.A. and Chiavassa, T.: Diffusion of molecules in the bulk of a low-density amorphous ice from molecular dynamics simulations. *Phys. Chem. Chem. Phys.* 17, 11455. DOI: 10.1039/c5cp00558b, 2015.
- 685 Gilbert, G. L., O'Neill, H. B., Nemeč, W., Thiel, C., Christiansen, H. H., and Buylaert, J. P.: Late Quaternary sedimentation and permafrost development in a Svalbard fjord-valley, Norwegian high Arctic. *Sedimentology*, 65(7), 2531–2558. <https://doi.org/10.1111/sed.12476>, 2018.
- 690 Gilbert, G., Instanes, A., Sinitsyn, A., and Aalberg, A.: Characterization of two sites for geotechnical testing in permafrost: Longyearbyen, Svalbard., *AIMS Geosci.*, 5(4): 868–885. <http://hdl.handle.net/11250/2632119>, 2019.
- Gilichinsky, D., and Wagener, S.: Microbial life in permafrost: A historical review. *Permafr. Periglac. Process*, 6(3), 243–250. <https://doi.org/10.1002/ppp.3430060305>, 1995.
- 695 Gonnee, M.E., Morris, P.J., Dulaiova, H., and Charette, M.A.: New perspectives on radium behavior within a subterranean estuary. *Mar. Chem.*, 109(3–4), 250–267. <https://doi.org/10.1016/j.marchem.2007.12.002>, 2008.



- Grant, K. M., Rohling, E. J., Ayalon, A., Ramsey, C. B., Satow, C., and Roberts, A. P.: Rapid coupling between ice volume and polar temperature over the past 150,000 years. *nature*, 491(7426), 744-747. <https://doi.org/10.1038/nature11593>, 2012.
- 700 Grundvåg, S.A., Jelby, M. E., Sliwiska, K.K., Nøhr-Hansen, H., Aadland, T., Sandvik, S. E., Tennvassås, I., Engen, T., and Olausen, S.: Sedimentology and palynology of the Lower Cretaceous succession of central Spitsbergen: integration of subsurface and outcrop data, *Nor. J. Geol.*, 99, 253–284. <https://doi.org/10.17850/njg006>, 2019.
- Harry, D. G., and Gozdzik, J. S.: Ice wedges: growth, thaw transformation, and palaeoenvironmental significance. *J. Quat. Sci.*, 3(1), 39-55. <https://doi.org/10.1002/jqs.3390030107>, 1988.
- 705 Henkemans, E.: Geochemical Characterization of Groundwaters, Surface Waters and Water-Rock Interaction in an Area of Continuous Permafrost Adjacent to the Greenland Ice Sheet, Kangerlussuaq, Southwest Greenland. A thesis presented to the University of Waterloo, Waterloo, Ontario, Canada. <http://hdl.handle.net/10012/10193>, 2016.
- Herut, B., Starinsky, A., Katz, A., and Bein, A.: The role of seawater freezing in the formation of subsurface brines, *Geochim. Cosmochim. Acta.*, 54, 13–21. [https://doi.org/10.1016/0016-7037\(90\)90190-V](https://doi.org/10.1016/0016-7037(90)90190-V), 1990.
- 710 Hivon, E. G., and Sego, D. C.: Distribution of saline permafrost in the Northwest Territories, Canada. *Can. Geotech. J.*, 30, 506– 514. <https://doi.org/10.1139/t93-043>, 1993.
- Hodson, A. J., Nowak, A., Hornum, M. T., Senger, K., Redeker, K., Christiansen, H. H., Jessen, S., Betlem, P., Thornton, S. F., Turchyn, A. V., Olausen, S., and Marca, A.: Sub-permafrost methane seepage from open-system pingos in Svalbard, *The Cryosphere*, 14, 3829–3842. <https://doi.org/10.5194/tc-14-3829-2020>, 2020.
- 715 Hornum, M. T., Hodson, A. J., Jessen, S., Bense, V., and Senger, K.: Numerical modelling of permafrost spring discharge and open-system pingo formation induced by basal permafrost aggradation. *The Cryosphere*, 14, 4627–4651. <https://doi.org/10.5194/tc-14-4627-2020>, 2020.
- Hsieh, T., Geibert, W., Stahl, H., Aleynik, D., and Henderson, G. M.: Using the radium quartet (228Ra, 226Ra, 224Ra, and 223Ra) to estimate water mixing and radium inputs in Loch Etive, Scotland. *Limnology and Oceanography*, 58(3), 1089-1102. <https://doi.org/10.4319/lo.2013.58.3.1089>, 2013.
- 720 Humlum, O., Instanes, A., and Sollid, J. L.: Permafrost in Svalbard: a review of research history, climatic background and engineering challenges. *Polar Res*, 22(2), 191-215. <https://doi.org/10.1111/j.1751-8369.2003.tb00107.x>, 2003.
- 725 Isaksen, K., Holmlund, P., Sollid, J. L., and Harris, C.: Three deep Alpine-permafrost boreholes in Svalbard and Scandinavia. *Permafr. Periglac. Process*, 12(1), 13-25. <https://doi.org/10.1002/ppp.380>, 2001.
- Iwahana, G., Cooper, Z. S., Carpenter, S. D., Deming, J. W., and Eicken, H.: Intra-ice and intra-sediment cryopeg brine occurrence in permafrost near Utqiagvik (Barrow). *Permafr. Periglac. Process*, 32(3), 427-446. <https://doi.org/10.1002/ppp.2101>, 2021.
- 730 James, M., Lewkowicz, A. G., Smith, S. L., and Miceli, C. M.: Multi-decadal degradation and persistence of permafrost in the Alaska Highway corridor, northwest Canada. *Environ. Res. Lett.*, 8(4), 045013. <http://dx.doi.org/10.1088/1748-9326/8/4/045013>, 2013.
- Jin, H. J., Chang, X. L., and Wang, S. L.: Evolution of permafrost on the Qinghai-Xizang (Tibet) Plateau since the end of the late Pleistocene. *J. Geophys.*, 112(F2). <https://doi.org/10.1029/2006JF000521>, 2007.



- 735 Jones, B. M., Kanevskiy, M. Z., Parsekian, A. D., Bergstedt, H., Ward Jones, M. K., Rangel, R. C., Hinkel, K. M., and Shur, Y.: Rapid Saline Permafrost Thaw Below a Shallow Thermokarst Lake in Arctic Alaska. *Geophys. Res. Lett.*, 50(22), e2023GL105552. <https://doi.org/10.1029/2023GL105552>, 2023.
- Keating, K., Binley, A., Bense, V., Van Dam, R. L., and Christiansen, H. H.: Combined geophysical measurements provide evidence for unfrozen water in permafrost in the Adventdalen valley in Svalbard. *Geophys. Res. Lett.*, 45(15), 7606-7614. <https://doi.org/10.1029/2017GL076508>, 2018.
- 740 Kiro, Y., Yechieli, Y., Voss, C.I., Starinsky, A., and Weinstein, Y.: Modeling radium distribution in coastal aquifers during sea level changes: the Dead Sea case. *Geochim. Cosmochim. Acta.*, 88, 237–254. <https://doi.org/10.1016/j.gca.2012.03.022>, 2012.
- Kiro, Y., Weinstein, Y., Starinsky, A., and Yechieli, Y.: Groundwater ages and reaction rates during seawater circulation in the Dead Sea aquifer. *Geochim. Cosmochim. Acta.*, 122, 17-35. <https://doi.org/10.1016/j.gca.2013.08.005>, 2013.
- 745 Kiro, Y., Weinstein, Y., Starinsky, A., and Yechieli, Y.: Application of radon and radium isotopes to groundwater flow dynamics: An example from the Dead Sea. *Chem. Geol.*, 411, 155-171. <https://doi.org/10.1016/j.chemgeo.2015.06.014>, 2015.
- 750 Kraemer, T.F., and Reid, D.F.: The occurrence and behavior of radium in saline formation water of the U.S. Gulf coast region. *Isotope Geosci.*, 2, 153-174. [https://doi.org/10.1016/0009-2541\(84\)90186-4](https://doi.org/10.1016/0009-2541(84)90186-4), 1984.
- Krishnaswami, S., Graustein, W. C., Turekian, K. K., and Dowd, J. F.: Radium, thorium and radioactive lead isotopes in groundwaters: Application to the in-situ determination of adsorption-desorption rate constants and retardation factors. *Water Resour. Res.*, 18(6), 1663-1675. <https://doi.org/10.1029/WR018i006p01663>, 1982.
- 755 Kwong, Y.T.J., and Gan, T.Y.: Northward migration of permafrost along the Mackenzie highway and climatic warming. *Clim. Change*, 26, 399–419. <https://doi.org/10.1007/BF01094404>, 1994.
- Lacelle, D., Fisher, D. A., Verret, M., and Pollard, W.: Improved prediction of the vertical distribution of ground ice in Arctic-Antarctic permafrost sediments. *Commun. Earth Environ.* 3(1), 1-12. <https://doi.org/10.1038/s43247-022-00367-z>, 2022.
- 760 Li, G., Zhang, M., Pei, W., Melnikov, A., Khristoforov, I., Li, R., and Yu, F.: Changes in permafrost extent and active layer thickness in the Northern Hemisphere from 1969 to 2018. *Sci. Total Environ.*, 804, 150182. <https://doi.org/10.1016/j.scitotenv.2021.150182>, 2022.
- Lønne, I. and Nemeč, W.: High-arctic fan delta recording deglaciation and environment disequilibrium, *Sedimentology*, 51, 553–589. <https://doi.org/10.1111/j.1365-3091.2004.00636.x>, 2004.
- 765 Mackay J. R.: Downward water movement into frozen ground, western arctic coast, Canada. *Can. J. Earth Sci.* 20(1): 120-134. <https://doi.org/10.1139/e83-012>, 1983.
- Mackay, J. R.: Ice-Wedge Cracks, Western Arctic Coast. *Can. Geogr.*, 33(4), 365-368. <https://doi.org/10.1111/j.1541-0064.1989.tb00923.x>, 1989.
- Mackay, J. R., and Dallimore, S. R.: Massive ice of the Tuktoyaktuk area, western Arctic coast, Canada. *Can. J. Earth Sci.*, 29(6), 1235-1249. <https://doi.org/10.1139/e92-099>, 1992.
- 770 Marion, G. M.: Freeze-Thaw Processes and Soil Chemistry (No. CRRELSR9512), 1995.



- Marsh, P., and Woo, M. K.: Infiltration of meltwater into frozen soils in a continuous permafrost environment. In Proceedings of the sixth international conference on permafrost, Vol. 1, pp. 443-448. Beijing: South China University of Technology Press, 1993.
- 775 Mathieu, G. G., Biscaye, P. E., Lupton, R. A., and Hammond, D. E.: System for measurement of  $^{222}\text{Rn}$  at low levels in natural waters. *Health Phys.*, 55(6), 989-992, 1988.
- Moore W. S.: Large groundwater inputs to coastal waters revealed by  $^{226}\text{Ra}$  enrichments. *Nature*, 380, 612–614. <https://doi.org/10.1038/380612a0>, 1996.
- Moore, W. S., and Arnold, R.: Measurement of  $^{223}\text{Ra}$  and  $^{224}\text{Ra}$  in coastal waters using a delayed coincidence counter. *J. Geophys. Res. Oceans*, 101(C1), 1321-1329. <https://doi.org/10.1029/95JC03139>, 1996.
- 780 Moore, W.S.: Sources and fluxes of submarine groundwater discharge delineated by radium isotopes. *Biogeochemistry* 66, 75–93, <https://doi.org/10.1023/B:BIOG.0000006065.77764.a0>, 2003.
- Mulrooney, M.J., Larsen, L., Van Stappen, J., Rismyhr, B., Senger, K., Braathen, A., Olausen, S., Mørk, M.B.E., Ogata, K. and Cnudde, V.: Fluid flow properties of the Wilhelmøya Subgroup, a potential unconventional  $\text{CO}_2$  storage unit in central Spitsbergen. *Nor. J. Geol.* 85-116. <https://doi.org/10.17850/njg002>, 2018.
- 785 Obu, J., Westermann, S., Bartsch, A., et al.: Northern Hemisphere permafrost map based on TTOP modelling for 2000–2016 at 1 km<sup>2</sup> scale. *Earth-Sci Rev.* 193, 299-316. <https://doi.org/10.1016/j.earscirev.2019.04.023>, 2019.
- Ogata, K., Senger, K., Braathen, A., Tveranger, J., and Olausen, S.: The importance of natural fractures in a tight reservoir for potential  $\text{CO}_2$  storage: a case study of the upper Triassic–middle Jurassic Kapp Toscana Group (Spitsbergen, Arctic Norway). Geological Society, London, Special Publications, 374(1), 395-415. <https://doi.org/10.1144/SP374.9>, 2014.
- Opel, T., Meyer, H., Wetterich, S., Laepple, T., Dereviagin, A., and Murton, J. Ice wedges as archives of winter paleoclimate: A review. *Permafr. Periglac. Process*, 29(3), 199-209. <https://doi.org/10.1002/ppp.1980>, 2018.
- Osterkamp, T. E., and Romanovsky, V. E.: Evidence for warming and thawing of discontinuous permafrost in Alaska. *Permafr. Periglac. Process*, 10(1), 17-37. [https://doi.org/10.1002/\(SICI\)1099-1530\(199901/03\)10:1<17::AID-PPP303>3.0.CO;2-4](https://doi.org/10.1002/(SICI)1099-1530(199901/03)10:1<17::AID-PPP303>3.0.CO;2-4), 1998.
- 795 Rama and Moore, W.: Mechanism of transport of U-Th series radioisotopes from solids into ground water. *Geochimica et Cosmochimica Acta*, 48(2), 395-399. [https://doi.org/10.1016/0016-7037\(84\)90261-8](https://doi.org/10.1016/0016-7037(84)90261-8), 1984.
- Rotem, D., Lyakhovskiy, V., Christiansen, H. H., Harlavan, and Weinstein, Y.: Permafrost saline water and Early to mid-Holocene permafrost aggradation in Svalbard, *The Cryosphere*, 17, 3363–3381. <https://doi.org/10.5194/tc-17-3363-2023>, 2023.
- 800 Rotem, D., Weinstein, Y., Christiansen, H. H., Sültenfuß, J., and Hodson, A.: Ra isotope perspective on the hydrology and continuity of permafrost in the high Arctic. *Sci. Total Environ.*, 950, 175412. <https://doi.org/10.1016/j.scitotenv.2024.175412>, 2024.
- 805 Sheshukov, A. Y., and Nieber, J. L.: One-dimensional freezing of non-heaving unsaturated soils: Model formulation and similarity solution. *Water Resour. Res.*, 47(11). <https://doi.org/10.1029/2011WR010512>, 2011.
- Solomatin, V. I., and Xu, X.: Water migration and ice segregation in the transition zone between thawed and frozen soil. *Permafr. Periglac. Process*, 5(3), 185-190. <https://doi.org/10.1002/ppp.3430050307>, 1994.



- Stephani, E., Drage, J., Miller, D., Jones, B. M., and Kanevskiy, M.: Taliks, cryopegs, and permafrost dynamics related to channel migration, Colville River Delta, Alaska. *Permafr. Periglac. Process*, 31(2), 239-254. <https://doi.org/10.1002/ppp.2046>, 2020.
- 810 Suksi, J. and Rasilainen, K.: On the Role of  $\alpha$ -Recoil in Uranium Migration - Some Findings from the Palmottu natural Analogue Site, SW Finland. *Radiochim. Acta*, 74(s1), 297-302. <https://doi.org/10.1524/ract.1996.74.special-issue.297>, 1996.
- 815 Vinson, D.S., Tagma, T., Bouchaou, L., Dwyer, G.S., Warner, N.R., and Vengosh, A.: Occurrence and mobilization of radium in fresh to saline coastal groundwater inferred from geochemical and isotopic tracers (Sr, S, O, H, Ra, Rn). *Appl. Geochem.* 38 (2013) 161–175. <http://dx.doi.org/10.1016/j.apgeochem.2013.09.004>, 2013.
- Wang, S., Wang, Q., Xu, J., and Ding, J.: Effect of freeze-thaw on freezing point and thermal conductivity of loess. *Arab. J. Geosci.*, 13:206. <https://doi.org/10.1007/s12517-020-5186-2>, 2020.
- 820 Wang, C., Li, S., Lai, Y., Chen, Q., He, X., Zhang, H., and Liu, X.: Predicting the Soil Freezing Characteristic From the Particle Size Distribution Based on Micro-Pore Space Geometry. *Water Resour. Res.*, 58(1), e2021WR030782. <https://doi.org/10.1029/2021WR030782>, 2021.
- Weinstein, Y., Rotem, D., Kooi, H., Yechieli, Y., Sültenfuß, J., Kiro, Y., Harlavan, Y., Feldman, M., and Christiansen, H. H.: Radium isotope fingerprinting of permafrost-applications to thawing and intra-permafrost processes. *Permafr. Periglac. Process*, 30(2), 104-112. <https://doi.org/10.1002/ppp.1999>, 2019.
- 825 Weinstein, Y., Friedheim, O., Odintsov, L., Harlavan, Y., Nuriel, P., Lazar, B., Burg, A.: Using radium isotopes to constrain the age of saline groundwater, implications to seawater intrusion in aquifers. *J. Hydrol.*, 598, 126412. <https://doi.org/10.1016/j.jhydrol.2021.126412>, 2021.
- Yershov, E.D.: *General Geocryology*. English ed. Cambridge, UK: Cambridge University Press.
- 830 Zhang, M., Zhang, X., Lu, J., Pei, W., and Wang, C. 2018. Analysis of volumetric unfrozen water contents in freezing soils. *Exp. Heat Transf.*, 32(5), 426–438. <https://doi.org/10.1080/08916152.2018.1535528>, 1998.